Methods in Oceanography 10 (2014) 44–69

Contents lists available at ScienceDirect

Methods in Oceanography

journal homepage: www.elsevier.com/locate/mio

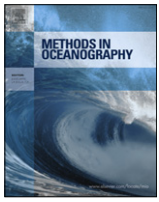

Full length article

Dissipation measurements using temperature microstructure from an underwater glider

Algot K. Peterson *, Ilker Fer

Geophysical Institute, University of Bergen, Allégaten 70, 5007 Bergen, Norway

ARTICLE INFO

Article history:
Received 16 December 2013
Received in revised form
9 May 2014
Accepted 13 May 2014
Available online 17 June 2014

Keywords:
Turbulence
Batchelor spectrum
Kraichnan spectrum
Faroe Bank Channel
Glider
Temperature microstructure

ABSTRACT

Microstructure measurements of temperature and current shear are made using an autonomous underwater glider. The glider is equipped with fast-response thermistors and airfoil shear probes, providing measurements of dissipation rate of temperature variance, χ, and of turbulent kinetic energy, ε, respectively. Furthermore, by fitting the temperature gradient variance spectra to a theoretical model, an independent measurement of ε is obtained. Both Batchelor (ε_B) and Kraichnan (ε_K) theoretical forms are used. Shear probe measurements are reported elsewhere; here, the thermistor-derived ε_B and ε_K are compared to the shear probe results, demonstrating the possibility of dissipation measurements using gliders equipped with thermistors only. A total of 152 dive and climb profiles are used, collected during a one-week mission in the Faroe Bank Channel, sampling the turbulent dense overflow plume and the ambient water above. Measurement of ε with thermistors using a glider requires careful consideration of data quality. Data are screened for glider flight properties, measurement noise, and the quality of fits to the theoretical models. Resulting dissipation rates from the two independent methods compare well for dissipation rates below 2×10^{-7} W kg^{-1}. For more energetic turbulence, thermistors underestimate dissipation rates significantly, caused primarily by increased uncertainty in the time response correction. Batchelor and Kraichnan spectral models give very similar results. Concurrent measurements of ε and χ are used to compute the dissipation flux coefficient Γ (or so-called apparent mixing efficiency). A wide range of values is found, with a mode value of $\Gamma \approx 0.14$, in agreement with previous studies. Gliders prove to be

* Corresponding author.
E-mail address: Algot.Petersson@gfi.uib.no (A.K. Peterson).

http://dx.doi.org/10.1016/j.mio.2014.05.002

suitable platforms for ocean microstructure measurements, complementary to existing methods.

1. Introduction

Direct measurements of turbulent mixing in the ocean require datasets of variables such as small-scale temperature or current shear sampled at high-frequency. Traditionally, such data are acquired using loosely-tethered profilers, deployed repeatedly off a ship's side (Lueck et al., 2002). This method provides data with little disturbance from vibrations, and repeated profiles can be made relatively fast. However, dedicated ship time is expensive, and microstructure surveys are sporadic. As an alternative, equipping underwater gliders with turbulence sensors facilitates continuous sampling on a low-vibration platform (Fer et al., 2014).

A glider is an autonomous vehicle that moves by changing its buoyancy, and can receive navigational instructions remotely via satellite. The wings, and to a lesser extent a tail fin, translate vertical motion into horizontal motion. This causes the glider to move through the water column in a vertical sawtooth pattern, resulting in quasi-vertical profiles. Dedicated ship time is not needed, making gliders a potentially very useful platform for turbulence measurements. Another benefit of gliders as an instrument to sample ocean microstructure is their ability to collect data during extreme atmospheric forcing. During stormy conditions, conducting profiling from ships is hazardous, and such mixing events are thus rarely sampled.

The first attempt to obtain turbulent dissipation rates from a glider was based on an indirect method utilizing standard sensors of the glider: Beaird et al. (2012) analyzed a large dataset from Seaglider (University of Washington) deployments over three years around the Greenland–Iceland–Scotland ridge, and inferred dissipation rates from finescale vertical velocity and density measurements. Their method is based on a scaling of the turbulent kinetic energy (TKE) equation, and relies on a scaling constant that is site specific, and accurate vertical water velocity measurements from a glider flight model. Energy loss at viscous scales is inferred from the larger, energy-containing scales. The results from this method compared very well to a co-located microstructure survey from the Faroe Bank Channel (FBC), with an agreement to within a factor of two, when ε varied over several orders of magnitude. The method allowed Beaird et al. (2012) to remotely map turbulent mixing and identify turbulent hot-spots in the region using gliders.

The first test using a Slocum electric glider equipped with turbulence sensors was done by Wolk et al. (2009) in an approximately 20 m deep freshwater pond. The glider was equipped with a self-contained microstructure instrument package (MicroRider, Rockland Scientific Int., Canada) with shear probes and thermistors. The vertical speed of the glider was typically 10 cm s^{-1}, corresponding to 40 cm s^{-1} along the glider's path, suitable for shear probe measurements. Wolk et al. (2009) found the glider to be a favorable platform for turbulence measurements.

The first detailed measurements in the ocean from a glider equipped with shear probes were reported by Fer et al. (2014). A deep Slocum electric glider equipped with a MicroRider with two shear probes was deployed in the FBC. Dissipation rate measurements from the glider and a ship-based vertical microstructure profiler were analyzed and compared. Vibration levels of the glider were generally small, and did not interfere with measurements of small-scale turbulent quantities. The glider measurements were shown to be of high quality, with the exception of the turning depths of the glider, where Taylor's hypothesis becomes invalid. The shear probes were able to resolve dissipation rates of TKE, ε, down to 5×10^{-11} W kg^{-1}, comparable to the best tethered free-fall profilers. In the turbulent bottom layer of the FBC, average profiles of ε from the glider and the microstructure profiler agreed to within a factor of two, whereas higher in the water column averaged glider-derived values were up to 9 times larger than the ship-based measurements. The discrepancies were attributed to the different sampling scheme (glider's slanted path), spatial and temporal separation between the instruments,

and the intermittency of turbulence. Gliders were, however, concluded to be a suitable platform for ocean microstructure measurements.

The present study is based on the same experiment reported in Fer et al. (2014). In addition to shear probes, the MicroRider was equipped with two fast-response thermistors (FP07), providing an additional set of microstructure data. This allows us to compare two independent methods for turbulence measurements from the same platform. The aim of this study is to investigate the usefulness of turbulence gliders in a natural and energetic oceanographic environment (see Section 4), and to compare the results from two methods, based on velocity shear and temperature microstructure. Special emphasis is given to the glider's thermistor data, including spectral methods to measure the dissipation rates and quality screening, as the shear probe-derived data are already described in detail by Fer et al. (2014). We therefore give a summary of temperature gradient spectral forms in the next section.

2. Temperature gradient spectral forms

Stirring of a thermally stratified fluid creates thermal microfronts through strain (Ruddick et al., 2000). Thermal diffusion prevents the gradients from becoming infinitely sharp. Under the assumption of small-scale isotropy, the rate of decrease of thermal variance due to diffusion of heat, χ, is given by

$$\chi = 6\kappa_T \left\langle \left(\frac{\partial T'}{\partial z} \right)^2 \right\rangle, \tag{1}$$

where $\partial T'/\partial z$ is the small scale vertical temperature gradient; $\kappa_T \sim 1.4\times10^{-7}$ m^2 s^{-1} is the molecular thermal diffusivity; and the angled brackets indicate averaging over a statistically uniform segment.

Dissipation rate of TKE, ε, is the rate of loss of TKE per unit mass through viscosity to heat (Thorpe, 2007), and has units of W kg^{-1}. In an incompressible, homogeneous and isotropic flow,

$$\varepsilon = \frac{15}{2}\nu \left\langle \left(\frac{\partial u'}{\partial z} \right)^2 \right\rangle, \tag{2}$$

where ν is the kinematic viscosity; and $\partial u'/\partial z$ is the small scale shear. When shear probe measurements are available, ε can be directly obtained by integrating the shear wavenumber spectrum.

For a locally isotropic turbulent patch, a one-dimensional temperature gradient spectrum can be calculated from the small-scale temperature gradient. The area under this spectrum is proportional to χ. By fitting the observed temperature gradient spectrum to a theoretical model, ε can also be determined. The Batchelor (1959) model is a widely accepted form of the theoretical spectrum (e.g., Ruddick et al., 2000; Luketina and Imberger, 2001), but the model of Kraichnan (1968) has also been suggested. Nash and Moum (2002) found that the latter matched their observations more closely than the Batchelor form. Sanchez et al. (2011) also found the Kraichnan form to be in better agreement with their limnic measurements, particularly at high wavenumbers. Both models are applied in this study, and are described in the following.

Note that wavenumbers k in theoretical expressions are typically given in units of radians per meter, while wavenumbers in observed spectra are presented in units of cycles per meter (1 cpm = 2π radian per meter). Here, we use radian wavenumbers in the equations, but use cyclic wavenumbers in the figures, all denoted with k.

2.1. The Batchelor spectrum

Batchelor (1959) was the first to describe the spectrum of a scalar characterized by a large Prandtl number. The Prandtl number is the ratio of the kinematic viscosity to the thermal diffusivity, $Pr = \nu/\kappa_T$. Water temperature is such a scalar. For the viscous wavenumber range, Batchelor (1959) derived the following three-dimensional temperature spectrum:

$$\phi_T(k) = -\frac{\chi}{\zeta k} \exp\left(\frac{\kappa_T k^2}{\zeta} \right), \tag{3}$$

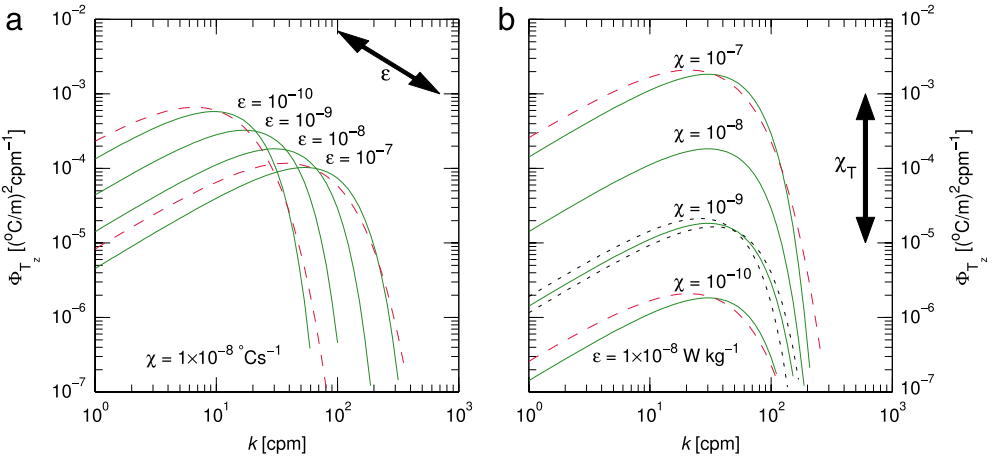

Fig. 1. Theoretical one-dimensional temperature gradient spectra for different values of (a) ε [W kg^{-1}] (with χ fixed at 10^{-8} °C s^{-1}) and (b) χ[°C s^{-1}] (with ε fixed at 10^{-8} W kg^{-1}). Batchelor spectra (green) are shown for four different values in each panel, whereas only two examples of the corresponding Kraichnan spectra (dashed red) are shown for clarity. The dotted black curves show the sensitivity to the value of q_B ($q_B = 3$, higher maximum at lower wavenumber, and $q_B = 5$, lower maximum at higher wavenumber). In all other Batchelor curves, $q_B = 3.7$.

where ζ is the average least principal strain rate, acting on scales smaller than the Kolmogorov wavenumber $k_K = (\varepsilon/\nu^3)^{1/4}$. The average least principal strain rate for flows at high Reynolds number is estimated from the Kolmogorov eddies,

$$\zeta = -\frac{1}{q_B}\left(\frac{\varepsilon}{\nu}\right)^{1/2}, \tag{4}$$

where q_B is a universal constant. The values of q_B reported in the literature vary; the range $q_B = 3.7 \pm 1.5$ is typical (Oakey, 1982). In this work, $q_B = 3.7$ is used, as was done by e.g., Nash et al. (1999) and Peters et al. (1988). Ruddick et al. (2000) and Kocsis et al. (1999) used $q_B = 3.4$, i.e. 8% smaller than the value used here. A higher value of q_B results in a higher maximum at a lower wavenumber, as shown in Fig. 1. A percentage error in q_B leads to twice the percentage error in ε (Dillon and Caldwell, 1980). By normalizing the wavenumber by the Batchelor wavenumber,

$$k_B = \left(\frac{\varepsilon}{\nu\kappa_T{}^2}\right)^{1/4}, \tag{5}$$

and the spectral level by $\chi(\nu/\varepsilon)^{1/2}k_B{}^{-1}$, the nondimensional form of Eq. (3) becomes

$$\frac{\phi_T(k)k_B}{\chi(\nu/\varepsilon)^{1/2}} = \frac{q_B k_B}{k}\exp[-q_B(kk_B{}^{-1})^2]. \tag{6}$$

The temperature spectrum can be converted to the temperature gradient spectrum, ϕ_{T_z}, by multiplying by k^2. Note that the spectrum in Eq. (3) is three-dimensional, indicated by the symbol ϕ. Typically, measured temperature spectra are one-dimensional, and the corresponding one-dimensional (indicated by the symbol Φ), isotropic form of the temperature gradient spectrum is (Bogucki et al., 2012)

$$\frac{\Phi_{T_z}(k)k_B}{\chi(\nu/\varepsilon)^{1/2}} = k^2\left(\frac{q_B k_B}{k}\exp[-q_B(kk_B{}^{-1})^2] + \pi^{1/2}q_B{}^{3/2}\{\mathrm{erf}[q_B{}^{1/2}kk_B{}^{-1}] - 1\}\right). \tag{7}$$

The temperature gradient spectrum is self-similar, and scales with k_B. The curve rises slowly up to the Batchelor cut-off, and rolls off exponentially for higher wavenumbers. In a log–log plot, changes in ε correspond to sliding the graph along a -1 slope, while changes in χ shifts the spectrum vertically, as illustrated in Fig. 1.

The subscript B will be used to denote the Batchelor temperature gradient spectra throughout, and to identify χ and ε derived from fits to the Batchelor form.

2.2. The Kraichnan spectrum

Kraichnan (1968) extended Batchelor's work by investigating the effects of fluctuations of the strain rates in time and space, keeping the k^{-1} behavior, but replaced the Gaussian factor in Eq. (3) by a simple exponential. The resulting expression for the one-dimensional isotropic temperature gradient spectrum is

$$\frac{\Phi_{T_z}(k)k_B}{\chi(\nu/\varepsilon)^{1/2}} = kk_Bq_K \exp[-(6q_K)^{1/2}kk_B{}^{-1}]. \tag{8}$$

Values of the universal constant q_K reported in the literature typically vary between 3.4 and 7.9. We use $q_K = 5.26$, following Bogucki et al. (2012). Similar to the Batchelor model, increasing q_K results in a larger spectral maximum at a lower wavenumber. For additional details on the theoretical spectra, the reader is referred to the review by Bogucki et al. (2012).

The subscript K is used throughout to denote the Kraichnan spectrum, and to identify χ and ε derived from fits to the Kraichnan model. Examples of Batchelor and Kraichnan spectra are shown in Fig. 1. Batchelor spectra are displayed for varying ε (Fig. 1(a)) and χ (Fig. 1(b)). For two selected curves in each panel, the corresponding Kraichnan spectra are also shown for comparison. The roll off at high wavenumbers in the Kraichnan model is less steep than in the Batchelor model. The sensitivity to q_B is also shown for the $\chi = 10^{-9}$ °C s^{-1} curve in Fig. 1(b), using $q_B = 3$ and $q_B = 5$ together with the default $q_B = 3.7$. The sensitivity to q_K in the Kraichnan spectrum is similar (not shown).

3. Field experiment

A physical oceanography research cruise to the Faroe Bank Channel (FBC) was conducted on board the research vessel Håkon Mosby, between 26 May and 14 June 2012. Hydrography and current profiles were made using the ship's CTD (conductivity, temperature, depth) system, equipped with a Sea-Bird Electronics (SBE) 911plus CTD and a pair of lowered acoustic Doppler current profilers (300 kHz RD Instrument Workhorse). Profiles of microstructure were made using a loosely tethered microstructure profiler, VMP2000 (VMP, Rockland Scientific). Additionally, two deep gliders were deployed during the cruise, each equipped with a CTD, and one equipped with turbulence instrumentation. The glider fitted with the turbulence sensors is the focus of this paper. A map of the location is shown in Fig. 2, marked with the glider tracks and the VMP stations. For a more complete description of the instrumentation, datasets and the oceanographic context, the reader is referred to Fer et al. (2014), Darelius et al. (2013) and Ullgren et al. (2014).

The glider used in this study is a Teledyne Webb Research Slocum Electric deep-glider (Jones et al., 2005). The glider is 1.8 m long, with a hull diameter of 22 cm and a wing span of 1 m. It has a mass of about 56 kg, and prior to deployment it is ballasted to be neutrally buoyant in a tank with seawater properties comparable to the deployment site. As a deep glider, it is designed for use down to 1000 m depth. The glider navigates using a rudder on the tail fin, and by moving the central battery pack to shift its center of gravity. Roll is adjusted by rotating the battery; pitch is adjusted by moving the battery back and forth. In the first dive, servo-controlled pitch was allowed to determine optimal battery positions during dives and climbs to maintain approximately $\pm 25^\circ$ pitch angles, recommended for nominal endurance. Then the servo was turned off, and the center battery position was manually set to these positions, in order to enable noise-free turbulence measurements.

The glider has an integrated SBE-41 CTD, but for microstructure measurements a Rockland Scientific MicroRider-1000LP (MR, hereafter) turbulence package is used. The package is mounted on top of the glider, and is equipped with two airfoil velocity shear probes, two fast response thermistors (FP07) and high resolution pressure, vibration and tilt sensors. Sensors are located 17 cm ahead and 16 cm off-axis from the glider's nose, minimizing flow deformation. Temperature, shear and vibration sensors sample at 512 Hz, while the other channels (pitch, roll and pressure) sample at 64 Hz. Equipping a glider with fast-response shear probes and thermistors allows turbulence measurements from two independent methods on the same platform.

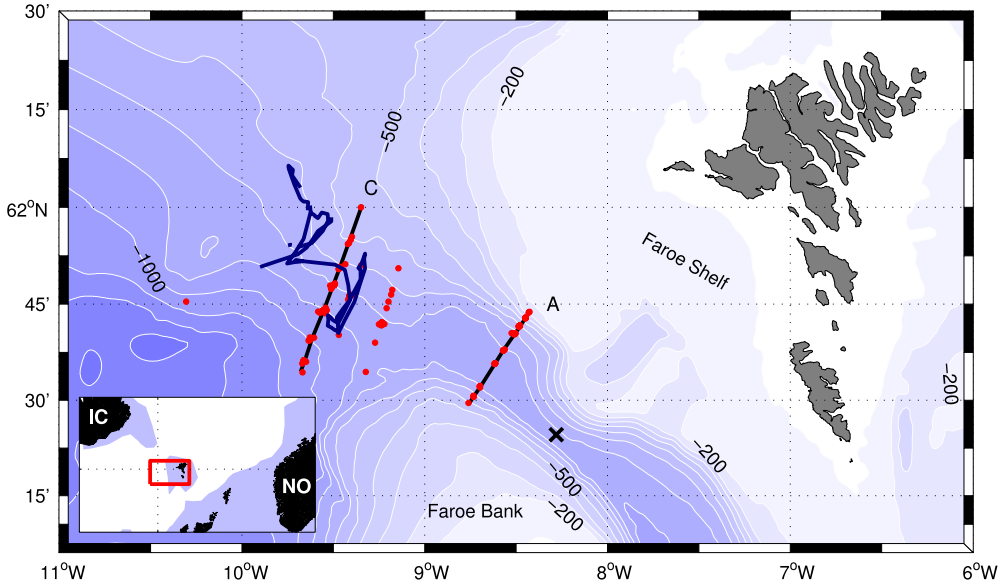

Fig. 2. Map of the field work location, including the Faroe Islands and the Faroe Bank Channel. Ship-based microstructure profiler casts are shown as red dots, and the glider track is shown in blue. Two sections, A and C, are highlighted by straight lines. Depth contours are shown every 100 m, the saddle point in the channel is indicated by a black cross. The insert map shows the 500 m isobath and the location relative to Iceland (IC) and Norway (NO).

4. Oceanographic setting

The FBC, with a sill depth of 840 m, is one of the two main passages across the Greenland–Scotland Ridge (GSR) where dense, cold deep water passes from the Nordic Seas to the North Atlantic (Fig. 2). Continuous measurements near the sill covering from 1995 to 2005 showed a total overflow volume flux of 2.7 $\pm$ 0.2 Sverdrup (1Sv $= 10^6$ m^3 s^{-1}), while the volume flux with temperatures lower than 3 °C was 1.7 $\pm$ 0.2 Sv (Hansen and Østerhus, 2007). The overflow is associated with oscillations with periods of 3–6 days, with 100–200 m thick domes of cold water flowing along the slope (Darelius et al., 2011). The highly turbulent bottom-attached overflow is approximately 100 m thick, and a turbulent, sheared and stratified interfacial layer of comparable thickness separates the overflow from the ambient water above (Fer et al., 2010). The structure of temperature and along-stream current speed in the overflow is visualized in Fig. 3. Two sections based on CTD and LADCP profiles from the present research cruise are displayed, one from the channel, and one from the open slope downstream. Their locations are indicated in Fig. 2. Both sections show the cold core of the plume leaning to the right hand slope, with high along-stream current speed, and large vertical gradients in both temperature and current speed.

A cross-stream circulation near the sill, where the flow is constrained by side walls of the channel, was observed by Johnson and Sanford (1992), caused by large frictional stress in the bottom boundary layer. At the interface they found cross-stream velocity in the opposite direction, suggesting a spiral pattern in the flow, causing significant mixing. Seim and Fer (2011) showed that a secondary circulation also existed farther downstream on the Iceland–Faroe slope, driven by the geostrophically-balanced component due to along-channel tilt of isopycnals. The first direct turbulence measurements in the FBC were performed by Fer et al. (2010). They found extraordinarily high dissipation rates in the interfacial layer and in the bottom part of the boundary layer, up to 10^{-5} W kg^{-1}. Measurements of mixing processes in the overflow are important in order to understand and quantify how the plume properties change as the plume descends the slope, and to determine the depth at which the overflow water becomes neutrally buoyant.

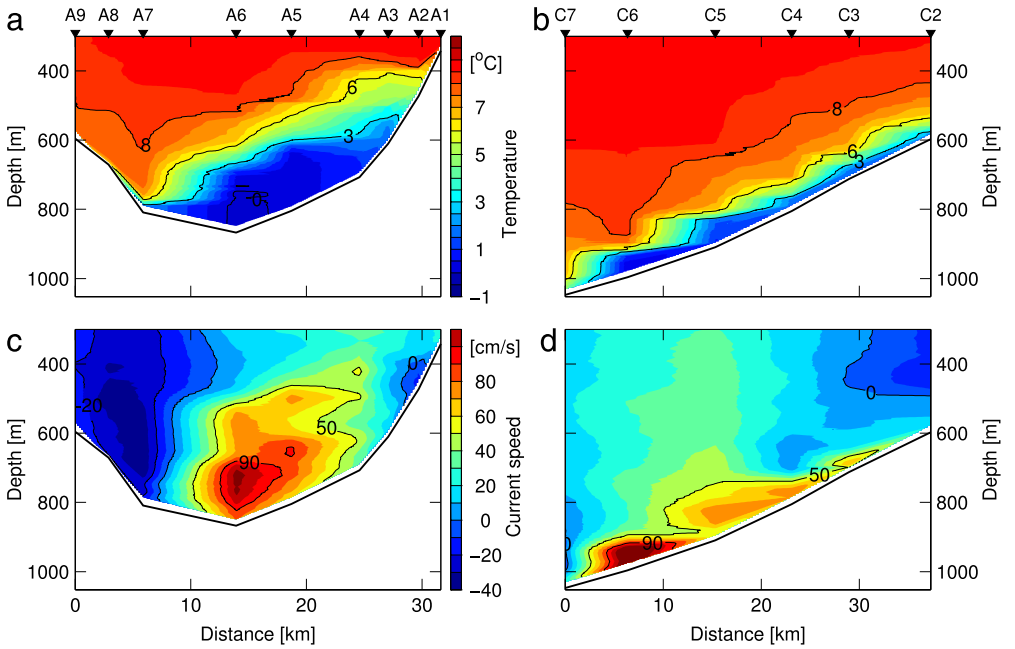

Fig. 3. Two sections of the overflow, color coded for ((a) & (b)) temperature and ((c) & (d)) along-stream current speed. North is to the right in all panels, and positive current speed is directed into the page. The top 300 m are not shown. The sections are located (Section A, (a) & (c)) in the channel and (Section C, (b) & (d)) on the open slope, as marked in Fig. 2. Arrowheads and numbered letters at the top mark the profile stations.

5. Data handling

5.1. Glider

The glider data are processed using the software kindly provided by Dr. Gerd Krahmann (GEOMAR, Germany). Raw files are first converted to physical units. Then GPS-fixes and internal navigational calculations are used to calculate a best guess of the glider's position. Top and bottom turns are identified from pressure records, and the time series are separated into dives and climbs. Unrealistic data are filtered out, and the remainder are interpolated to 1 s time-steps for all sensors.

Salinity is calculated from conductivity, temperature and pressure using the Gibbs SeaWater (GSW) Oceanographic Toolbox (McDougall and Barker, 2011). Potential density anomaly for surface reference pressure (σ_θ) is calculated from salinity and temperature, also using GSW.

The direction the glider moves relative to the horizontal, the glide angle, γ, is defined as the sum of the glider pitch angle, θ, and an 'angle of attack' (AOA), α, i.e. $\gamma = \theta + \alpha$. For high quality dissipation rate measurements, glider speed, U, and α must be accurately known. A hydrodynamic flight model, described in Merckelbach et al. (2010), is used to obtain the glider speed through water U, and α. The model uses the force balance along the glider's path. The force balance can be written as

$$F_B - F_g - \frac{\rho S_w U^2 \times [C_{D_0} + C_{D_1}\alpha^2]}{2\sin\gamma} = 0, \tag{9}$$

which is Eq. 13 of Merckelbach et al. (2010), corrected for a sign error. F_B is the net buoyancy force, $F_g = m_g g$ is the gravitational force for a glider of mass m_g, g is acceleration due to gravity, ρ is the in situ density, and S_w is the glider wing surface area. The total parasite and induced drag is determined by the coefficients C_{D_0} and C_{D_1}, respectively. C_{D_0} is the profile drag coefficient of the glider hull,

C_{D_1} is the sum of the induced drag coefficients of the wings and the hull. The net buoyancy force is given by

$$F_B = g\rho\{V_g[1 - c_h P + \alpha_T(T - T_0)] + \Delta V_{bp}\}, \tag{10}$$

where V_g is the glider volume, c_h is the hull compressibility, P is the water pressure, α_T is the thermal expansion coefficient, T is temperature, T_0 is a reference temperature, and ΔV_{bp} is the buoyancy change resulting from the buoyancy engine of the glider.

The angle of attack is obtained by numerical iteration of the expression

$$\alpha = \frac{C_{D_0} + C_{D_1}\alpha^2}{(a_w + a_h)\tan(\theta + \alpha)}, \tag{11}$$

where a_h and a_w are the lift-slope coefficients for the hull and wings, respectively.

For a deep Slocum glider, the optimized values of $C_{D_1} = 2.88$, $a_w = 3.7$, $a_h = 2.4$ rad^{-1} are reported in Merckelbach et al. (2010). The variables T, ρ, P, θ and ΔV_{bp} are measured by the glider, and $S_w = 0.1$ m^2 and $m_g \sim 56.4$ kg. The parameters C_{D_0}, c_h and V_g are calibrated for the glider equipped with the MicroRider by minimizing a cost function relative to the vertical velocity inferred from rate of change of pressure, w_p, using a non-linear least-squares method. For details on the optimization, see Fer et al. (2014). Average values (±one standard deviation) are $C_{D_0} = 0.14(\pm 0.02)$, $c_h = 6.1(\pm 0.2) \times 10^{-10}$ Pa^{-1}, and $V_g = 55(\pm 0.1) \times 10^{-3}$ m^{-3}. In their optimization, Fer et al. (2014) used the glider mass without the MR mass. The correct value should be approximately $m_g = 62.5$ kg. The associated error in the buoyancy force calculation is less than 10%, and is largely compensated for by the optimization of the free parameters. Reprocessing using the correct m_g results in identical average glider speeds, AOA, and dissipation rates within the measurement uncertainty. The drag coefficient here is higher than that reported in Merckelbach et al. (2010), consistent with the approximately 30% larger frontal area of a glider equipped with a MicroRider. Once the glider speed, U, and the glide angle are obtained, the vertical speed of the glider is computed as $w_g = U\sin(\theta + \alpha)$. The average glider along-path speed is $U = 39$ cm s^{-1} and $U = 43$ cm s^{-1}, and vertical speed is $w_g = 17$ cm s^{-1} and $w_g = 24$ cm s^{-1}, for dives and climbs, respectively, see Table 1 of Fer et al. (2014). The asymmetry in glider speed is not due to the MR, but the manually set central battery positions.

5.2. MicroRider

The time stamp, pressure (P) and temperature (T) records of the MR are corrected against the glider data. Along-path velocity, U, relative to the water, and the vertical velocity, w_g, are calculated as described in Section 5.1.

Dissipation rates of TKE are calculated using two different methods. One method involves direct measurements of velocity shear. Under the assumption of isotropic turbulence, dissipation rates can be calculated solely from high resolution profiles of velocity shear variance (Eq. (2)), by integrating the wavenumber spectrum. Because of difficulties in resolving scales smaller than the Kolmogorov length $l_K = (\varepsilon\nu^{-3})^{-1/4}$, the unresolved part of the velocity shear spectrum is accounted for by using an empirical turbulence spectrum (Nasmyth, 1970; Oakey, 1982). Additional details on the application of this method can be found in Fer et al. (2014). A subscript N (for Nasmyth) is used to denote dissipation rates derived from glider shear probes.

The second method involves the measurement of temperature microstructure. Time series from the two thermistors are divided into 12 s half-overlapping segments, corresponding to about 2.4 m vertical segment length. A fast Fourier transform (FFT) length corresponding to 4 s is chosen, and each FFT segment is detrended and Hanning-windowed before calculating the spectra. The segment and FFT length are identical to those used in the processing of the shear probe data. The frequency domain spectra, $\Phi(f)$, are converted to along-path wavenumber (k) domain using Taylor's frozen turbulence hypothesis and the glider speed through water, as $\Phi(k) = U\Phi(f)$ and $k = f/U$. For a typical $U \sim 0.4$ m s^{-1}, the FFT length is equivalent to a 1.6 m along-path distance.

Assuming isotropic turbulence as before, Eq. (1) can be used for glider measurements, using the temperature gradient along the glider's path, x,

$$\chi = 6\kappa_T \left\langle \left(\frac{\partial T'}{\partial x} \right)^2 \right\rangle. \tag{12}$$

The glider speed is used to convert time gradient to $\partial/\partial x$. The fast response thermistor FP07 on the MicroRider has a response time of about 12 ms (1 ms $\equiv 10^{-3}$ s), due to diffusion and attenuation of the signal in the boundary layer around the probe. The microstructure spectra are corrected using the dynamic response function $H^2(f) = (1 + (f/f_c)^2)^{-1}$, where $f_c = (2\pi\tau U^{-0.32})^{-1}$ is a speed-dependent cut-off frequency and $\tau = 12$ ms is the thermistor response time (Gregg and Meagher, 1995). The sensitivity of our results to the choice of time constant and the response correction function is discussed in Section 7.4.

The temperature profile needs to resolve the Batchelor wavenumber (Eq. (5)), or alternatively a sufficiently – but not completely – resolved gradient spectrum can be fitted to one of the universal forms given by Batchelor (1959) and Kraichnan (1968), as described in Section 2. We first obtain χ by integrating the observed Φ_{T_z} up to an upper wavenumber, k_u, determined as described in Section 5.3. The integrated part of the spectrum is significantly above the noise level. We obtained the noise spectrum, $\Phi_n(k)$, by averaging over the quiescent segments of our dataset. We apply a correction to χ for the unresolved variance for wavenumbers greater than k_u, following the relation in the appendix of Peters et al. (1988). We obtain the dissipation rate ε from the temperature microstructure using the maximum likelihood estimate (MLE) fit of the observed temperature gradient spectrum to a theoretical spectrum (Ruddick et al., 2000), constrained by the measured and corrected χ. This method allows inclusion of the noise spectrum $\Phi_n(k)$ in the theoretical spectrum $\Phi_{th}(k)$,

$$\Phi_{th}(k) = \Phi_{B,K}(k) + \Phi_n(k), \tag{13}$$

where $\Phi_{B,K}(k)$ is the Batchelor or Kraichnan spectrum, Eqs. (7) and (8), respectively. Only the part of the observed spectrum up to k_u is fitted.

An advantage of MLE over least squares, is that for non-Gaussian error distributions, the least squares method is often biased, while the MLE estimates are unbiased (Ruddick et al., 2000). The method also reduces the number of free parameters to adjust, since χ is constrained by the integrated temperature gradient spectrum. Only the Batchelor wavenumber k_B needs to be adjusted to fit the theoretical spectrum, given by Eq. (5), which gives the dissipation rate:

$$\varepsilon = k_B^4 \nu \kappa_T^2. \tag{14}$$

After data quality screening (Section 5.3), the results from the two thermistors are checked for consistency, and then averaged.

5.3. Data selection

The MLE fits are made in the portion of each spectrum uncontaminated by noise. The upper wavenumber, k_u, for integration of a temperature gradient spectrum is chosen as the lowest wavenumber where the measured spectrum equals 1.5 times the noise spectrum, or at the most, 200 cpm. There is no credibility in Φ_{T_z} measured by our system at higher wavenumbers. Furthermore, we require at least 5 data points before any fit is attempted.

Ruddick et al. (2000) introduce three rejection criteria for the MLE method, allowing poorly fitted spectra to be identified and discarded automatically. First, the integrated signal-to-noise ratio (SNR) is required to be greater than 1.3, before any fit is attempted. We arbitrarily set SNR > 1.5 as our threshold value, i.e., the spectral variance averaged up to k_u should be greater than 1.5 times that from the noise spectrum. Second, the mean absolute deviation (MAD) between the observed and the theoretical spectra, Φ_{obs} and Φ_{th}, must be sufficiently small. The deviations are summed up to the wavenumber k_u,

$$\mathrm{MAD} \equiv \frac{1}{n} \sum_{k_i=k_1}^{k_u} \left| \frac{\Phi_{obs}}{\Phi_{th}} - \left\langle \frac{\Phi_{obs}}{\Phi_{th}} \right\rangle \right|. \tag{15}$$

Following Ruddick et al. (2000), a data segment is rejected if MAD is greater than $2(2/d)^{1/2}$, where d is the degrees of freedom of the measured spectrum. This rejection limit is twice the MAD expected from a "perfect fit". A raw periodogram has $d = 2$. For 12 s segments with 4 s FFT length, $d = 6$, ignoring the effects of the 50% window overlapping and Hanning windowing.

To ensure that an observed spectrum resolves the sharp roll off of the theoretical spectra, a power-law fit (a straight line in log–log space) is made, which has no roll off. If the theoretical curves do not provide a significantly better fit than the power law, the segment should be rejected (Ruddick et al., 2000). The likelihood ratio (LR), which is the ratio of MLE of the power law fit to the MLE of the theoretical spectrum fit, is calculated as in Ruddick et al. (2000). If $\log_{10}$ (LR) is less than 2, the data segment is rejected, based on the recommendations of Ruddick et al. (2000). This criterion works well for power law fits with a negative slope. However, the slope is positive in the low wavenumber part of the theoretical spectra. When the roll off is located at high wavenumbers, the low wavenumber part of the spectrum increases linearly with k, consistent with the theoretical form. A power law fit will then have a positive slope, and may give a higher likelihood than the theoretical curve, even for a good fit to the theoretical form. We therefore apply the LR criterion only when the power law fit has a negative slope.

Fig. 4 shows two examples of observed temperature gradient spectra. The full profiles (below 500 m) of temperature and temperature gradient are shown, together with selected two 12 s segments for which the spectra are presented. Note that this is the segment length used in our data processing, and the spectra are not smoothed, band-averaged or ensemble-averaged over larger segments. The spectra are not exceptional in quality, and are representative of the dataset. The MLE fit of the Batchelor spectrum and Kraichnan spectrum are shown, and the straight lines represent the best power-law fit to each spectrum. Both the quiescent spectrum in Fig. 4(d) and the more energetic spectrum in Fig. 4(e) show good fits with well-resolved roll offs. The scatter in the spectra are typical for oceanic spectra derived for short segment lengths, and such spectra are not expected to adhere perfectly to the theoretical forms. Kraichnan's spectrum seems to give a better fit than the Batchelor model for high wavenumbers. This, however, is not true for all spectra.

Taylor's hypothesis assumes that an eddy does not change significantly as it advects past the measurement point. When the glider speed through water is comparable to the velocity scale of the largest eddies, Taylor's hypothesis is not valid. The relatively low speed and the slanted path of the glider require careful data selection. Following Fer et al. (2014), the ratio $R = U/u_t$, where U is the glider's along-path speed, and u_t is a turbulent velocity scale, is used to identify the segments that are suspect to Taylor's hypothesis. The measured dissipation rates are used to infer a turbulent velocity scale, $u_t \sim (\varepsilon l)^{1/3}$. By substituting the turbulent length scale l by the Ozmidov length scale,

$$L_O = (\varepsilon/N^3)^{1/2}, \tag{16}$$

we obtain

$$u_t = (\varepsilon/N)^{1/2}. \tag{17}$$

Here, N is the buoyancy frequency, approximated using the observed potential density anomaly profile, $\sigma_\theta(z)$,

$$N(z) = \left(-\frac{g}{\rho_0}\frac{\partial \sigma_\theta}{\partial z}\right)^{1/2}, \tag{18}$$

where ρ_0 is a reference density.

An estimate of the noise level for ε and χ derived from temperature microstructure is calculated. A synthetic spectrum is assigned spectral values 1.55 times our measured noise spectrum, just above our minimum requirement of SNR > 1.5. Then an MLE fit is made to the Batchelor form, giving the lower limits for $\varepsilon = 5 \times 10^{-11}$ W kg^{-1} and $\chi = 1 \times 10^{-11}$ °C s^{-1}. Values lower than this are not resolved by the thermistors, and are excluded from analysis.

The cumulative spectral contribution to χ for different values of ε is shown in Fig. 5. It describes the fraction of χ resolved, when Φ_{T_z} is integrated up to a wavenumber k. Also shown is the spectral response function using a typical glider speed of 0.4 m s^{-1}. The inverse of the response function is the

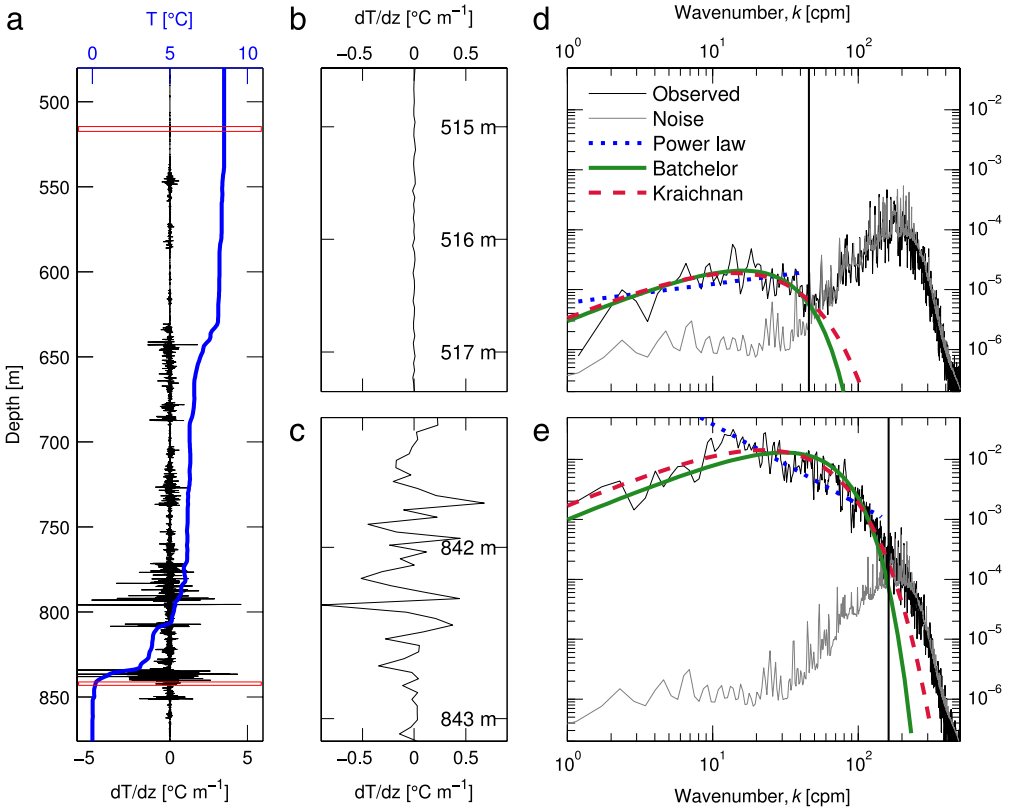

Fig. 4. Temperature microstructure from an example profile. Profiles of (a) temperature (blue) and temperature gradient dT/dz (black), and blow up of two 12 s segments of dT/dz from (b) a quiescent and (c) an energetic part of the profile (marked as red rectangles in a). In this presentation the time series are averaged to 4 Hz for clarity. The respective temperature gradient spectra of the two segments ((d) & (e), black) are fitted to a power law (blue dotted line), the Batchelor spectrum (green) and the Kraichnan spectrum (red). The model noise spectrum is indicated (gray). Both spectra show a good fit, and are accepted according to our criteria. In (d), MAD $= 0.33$ and $\varepsilon = 1.3 \times 10^{-9}$ W kg^{-1}, and in (e), MAD $= 0.44$, $\log_{10}(\mathrm{LR}_B) = 86.5$ and $\varepsilon = 1.8 \times 10^{-8}$ W kg^{-1}. The $\log_{10}$ (LR) criterion is not applicable in (d), since the slope of the power law fit is positive (as explained in the text). The vertical black lines in (d) and (e) indicate k_u, up to which the fits are made. (For interpretation of the references to color in this figure legend, the reader is referred to the web version of this article.)

correction needed to compensate for the attenuation in the thermistors power response. For turbulent segments, ε is poorly resolved using thermistors. For $\varepsilon = 10^{-7}$ W kg^{-1}, χ must be corrected by a factor of 2 already at approximately 30 cpm, where the response correction on the Φ_{T_z} is approximately a factor of 4. These corrections are too large, (and particularly the response correction is very uncertain,) and ε measurements become inaccurate. We exclude ε_B and ε_K greater than 2×10^{-7} W kg^{-1} from the analysis. Note that ε_N is properly resolved, and $\varepsilon_N > 2 \times 10^{-7}$ are only excluded when comparing to $\varepsilon_{B,K}$, for consistency.

In summary, average flight properties (U, w_g, γ, AOA), turbulent parameters ε and χ, and $R = U/u_t$ are calculated for each 12 s segment. Segments are rejected and excluded from analysis when any of the following conditions are fulfilled (see also Fer et al., 2014): $R \leq 15$ for dives and $R \leq 20$ for climbs, AOA ≥ 5, $|w_g| < 0.05$ m s^{-1}, $|w_g| > 0.5$ m s^{-1}, SNR < 1.5, MAD $> 2(2/\mathrm{d})^{1/2}$, $\log_{10}(\mathrm{LR}) < 2$, $\varepsilon < 5 \times 10^{-11}$ W kg^{-1}, $\varepsilon > 2 \times 10^{-7}$ W kg^{-1} or $\chi < 1 \times 10^{-11}$ °C s^{-1}. After data screening, thermistor data was left with approximately 46 000 out of the original 62 000 segments for analysis, distributed as 63% dives and 37% climbs. Shear probe data is reduced from approximately 73 000 to 55 000 data points after data screening, and further down to 51 800 when $\varepsilon_N > 2 \times 10^{-7}$ W kg^{-1} are excluded for comparison with $\varepsilon_{B,K}$.

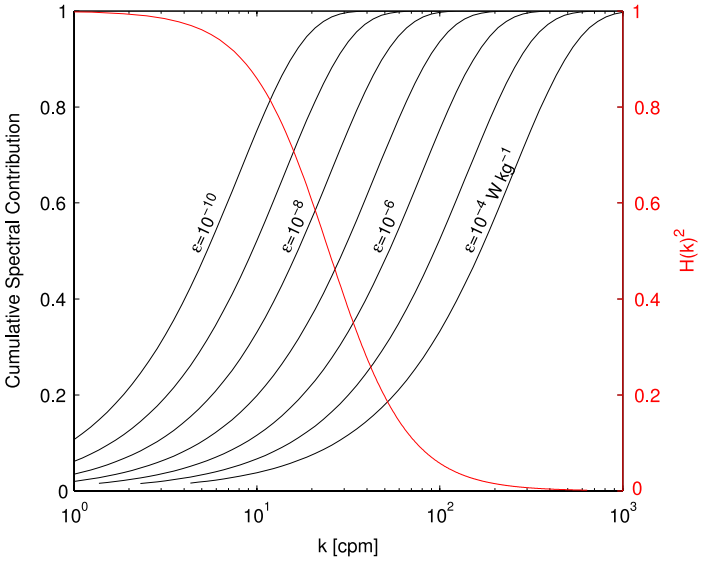

Fig. 5. Relative cumulative spectral contribution to χ as a function of wavenumber for the Batchelor spectrum with $q_B = 3.7$, and ε increasing from 10^{-10} to 10^{-4} W kg^{-1}. For all spectral contribution curves, $\chi = 10^{-7}$ °C s^{-1}. The spectral response function for a glider speed of 0.4 m s^{-1} is shown in red. (For interpretation of the references to color in this figure legend, the reader is referred to the web version of this article.)

6. Results

6.1. Average spectra

Observed temperature gradient spectra span a wide range of turbulence levels, from the quiescent interior to the highly turbulent plume interfacial and bottom boundary layers. An overview of all spectra from segments which passed the quality screening is shown in Fig. 6, where gray shading indicates the span of spectral values at selected percentiles. The average spectrum between the 45–55th percentiles shows a shape similar to the theoretical Batchelor and Kraichnan forms in the dissipation subrange, between 5 and 100 cpm. We restricted the example average spectrum to a narrow percentile range because averaging over a large range of ε and χ will distort the spectral shape (i.e., individual spectra are not sampled from a homogeneous turbulent patch). For the low wavenumbers, in the viscous-convective subrange, the observed spectrum has a gentler slope than the theoretical forms. The dissipation rates obtained from the fits are $\varepsilon_B = 1.4 \times 10^{-8}$ W kg^{-1} and $\varepsilon_K = 1.3 \times 10^{-8}$ W kg^{-1}, and $\chi = 2.6 \times 10^{-8}$ °C s^{-1}.

The range and quality of the observed temperature gradient spectra are again demonstrated in Fig. 7, where spectra are averaged in decadal bins of χ and ε in the range 10^{-6}–10^{-10} for both ε (W kg^{-1}) and χ (°C s^{-1}). Thousands of spectra are averaged, see Table 1 for details. The averaged spectra are displayed with respect to both frequency and wavenumber. Fits of the Batchelor form to selected averaged spectra are also shown. In a given χ or ε bin, the corresponding parameter spans one order of magnitude (by definition) and the other parameter can vary even more. The average spectrum is thus not representative of a homogeneous patch with given ε and χ, and will differ from the theoretical form. The expected variability in the spectral form for each bin can be estimated by the Batchelor spectrum calculated using the observed variability in ε and χ. The dashed envelope in Figs. 7(b) and 7(d) shows the Batchelor spectrum for ± 0.5 standard deviation variability. The variable glider speed also distorts the spectral shape, but this is found to be negligible (variability in a given bin is less than 5%).

All presented average or individual spectra of temperature gradient closely follow the Batchelor or Kraichnan forms in the diffusive subrange where the spectra roll off. These are the scales that contain

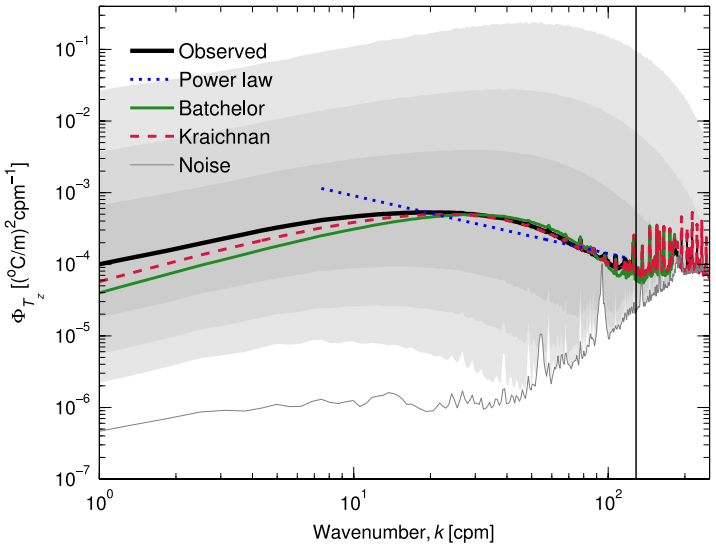

Fig. 6. Overview of the temperature gradient spectra from the 46 000 segments that are of good data quality. The gradually darker gray shadings are defined by the 2nd/98th, 10th/90th and 25th/75th percentile values at each wavenumber, respectively. A mean spectrum of all spectral values within 5% of the median is shown in black together with the MLE-fitted Batchelor spectrum (green), Kraichnan spectrum (dashed red) and a power law fit (dotted blue). The noise spectrum is shown by the gray line. The vertical black line indicates k_u, the wavenumber up to which the fits to the average spectrum are made. The values obtained from the MLE fit are $\varepsilon_B = 1.4 \times 10^{-8}$ W kg^{-1}, $\varepsilon_K = 1.3 \times 10^{-8}$ W kg^{-1} and $\chi = 2.6 \times 10^{-8}$ °C s^{-1}.

Table 1
Number of segments with good Φ_{T_z}-spectra in decadal bins of ε and χ, used for calculating bin averaged spectra in Fig. 7. The bin range is in units of W kg^{-1} for ε and °C s^{-1} for χ.

Bin range	ε-binned	χ-binned
$[10^{-10}\ 10^{-9}]$	6 587	4 635
$[10^{-9}\ 10^{-8}]$	16 374	12 007
$[10^{-8}\ 10^{-7}]$	19 516	13 708
$[10^{-7}\ 10^{-6}]$	2 941	9 513

most of the gradient variance. At the lower wavenumbers in the viscous-convective subrange with k^{+1} slope, spectral amplitudes are up to a factor of 2 greater than the theoretical shapes. Similar deviations are reported extensively in the literature (Dillon and Caldwell, 1980; Nash and Moum, 2002; Oakey, 1982; Sanchez et al., 2011), especially for small Cox numbers ($C_x = \langle dT'/dz \rangle^2 / \langle dT/dz \rangle^2$). Typically, the deviations are attributed to remnant background vertical temperature structure (Dillon and Caldwell, 1980; Nash and Moum, 2002), or, inverse cascade of a fraction of the spectral peak to lower wavenumbers (Nash and Moum, 2002).

6.2. Shear probe and thermistor comparison

6.2.1. Average profiles

In order to present and quantify the performance of the thermistors in measuring ε, a comparison to shear probes is first attempted in the average sense. This also ensures that sufficient sampling and averaging is made over the 3–6 day period oscillation which dominates the variability at the site (see Section 4). Survey averages are made from the glider thermistor data (Batchelor, ε_B, and Kraichnan, ε_K, MLE fits), and shear probe data (Nasmyth, ε_N) from the glider. To determine the vertical bin size for survey averages, a run-length test for uncorrelatedness is performed, as described by Gregg

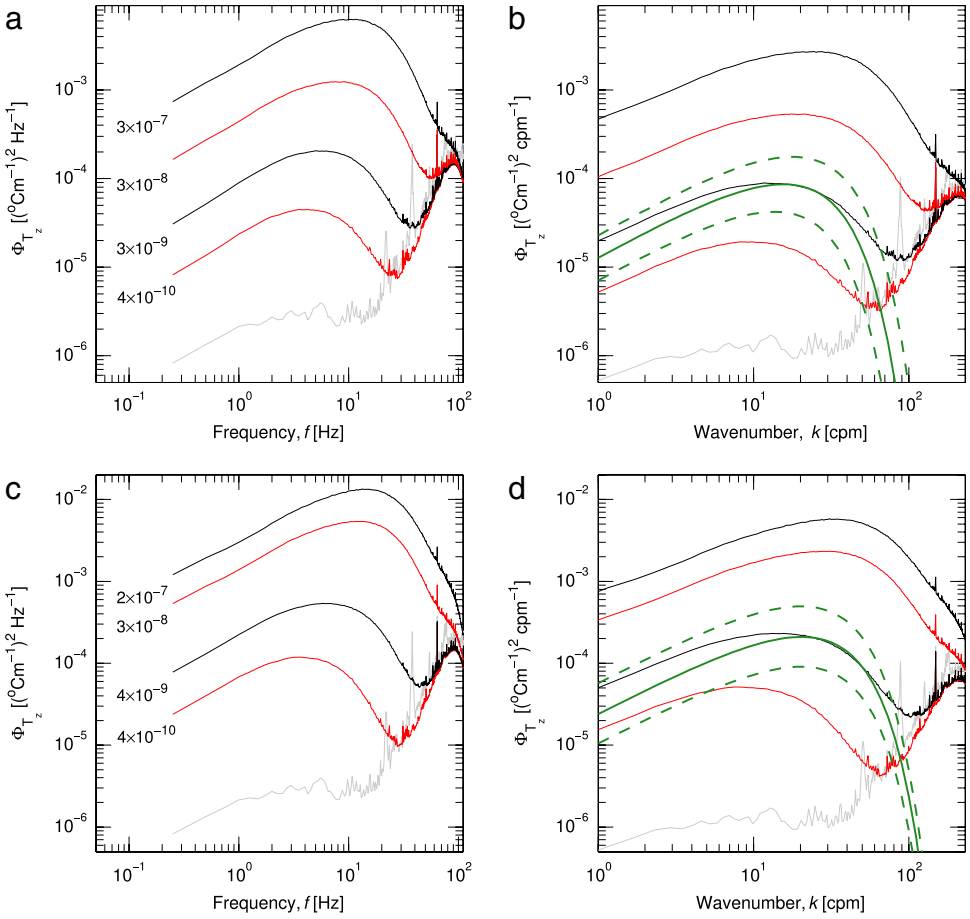

Fig. 7. Temperature gradient spectra, averaged in decadal bins with respect to ((a) & (b)) χ and ((c) & (d)) ε between 10^{-10} and 10^{-6}. Noise spectra are shown in gray. Panels (a) and (c) show frequency spectra, while (b) and (d) show wavenumber spectra. The average values of χ [°C s^{-1}] and ε [W kg^{-1}] in each bin are given in panels (a) and (c), respectively. For clarity, a Batchelor fit (green) is shown for only one mean spectrum in each of panels (b) and (d). The dashed Batchelor spectra envelop 0.5 standard deviation variability in ε and χ in the chosen decadal bin. (For interpretation of the references to color in this figure legend, the reader is referred to the web version of this article.)

et al. (1993). The test determines, within a 5% significance level, whether consecutive values are correlated or not. We perform the test for glider-derived dissipation rates of TKE, from both shear and temperature gradient spectra. Only data from depths between 100 m and 250 m are used, to ensure uniform stratification. For bin sizes of 1–2 m, over 50% of the profiles are rejected as correlated, but with increasing bin size, the rejection ratio reduces to approximately 10% for 10 m bins. When the bin size is further increased to 15 m, the rejection percentage is below the 5% significance level. Thus 15 m bin averages are treated as uncorrelated, and the profiles are averaged in 15 m vertical bins. The test shows similar results for both temperature- and shear-derived ε.

Survey-averaged ε profiles are calculated relative to the 3 °C-isotherm depth and as height above bottom (HAB), and are shown in Fig. 8. The 3 °C isotherm is a useful identifier of the interface between the dense plume and the interfacial layer above. Two versions of the shear-derived dissipation rate (ε_N) profiles are shown; one profile excludes $\varepsilon_N > 2 \times 10^{-7}$ W kg^{-1} to be consistent for comparison with thermistor data, the other profile includes all quality screened ε_N in averaging. The latter is shown, because ε is resolved by the shear probes, to show the actual turbulence levels in the bottom

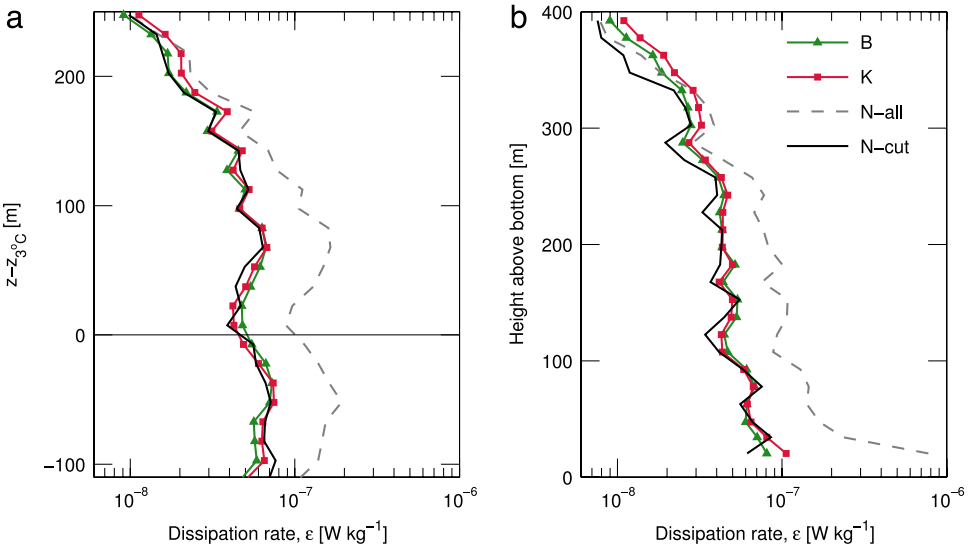

Fig. 8. Survey-averaged profiles of dissipation rates of TKE from the glider using shear (Nasmyth; values of $\varepsilon > 2 \times 10^{-7}$ excluded for comparison, in black, and the complete version for reference, dashed gray) and temperature microstructure; Batchelor fit (green) and Kraichnan fit (red). Data are vertically averaged in 15 m bins with respect to (a) the 3 °C isotherm, indicative of the dense plume interface, and (b) height above bottom (HAB). (For interpretation of the references to color in this figure legend, the reader is referred to the web version of this article.)

boundary layer, and in the turbulent interface. When $\varepsilon_N > 2 \times 10^{-7}$ W kg^{-1} are excluded from averaging, the agreement between the methods is very good. For low dissipation rates, above 300 m HAB, the two versions of ε_N agree closely. Closer to the bottom, the offset between the two shear profiles increases, as expected because of the increasing dissipation rates. As a result of the thermistors' inability to resolve the most energetic turbulence, the mean profiles of $\varepsilon_{B,K}$ show only a slight increase in dissipation rates towards the bottom.

A survey-averaged profile of χ is shown in Fig. 9. (Profiles for χ are identical for Batchelor and Kraichnan, because χ is obtained by integrating the temperature gradient spectrum to constrain the theoretical spectra.) There is a gradual increase in χ towards the bottom. The survey average relative to the 3 °C isotherm reveals a peak in χ at 3 °C, about one order of magnitude higher than just 100 m above or below. The 3 °C isotherm is in the stratified interfacial layer (Fig. 4), where the background temperature gradient is large and the current shear is strong. The increase in χ in this layer is consistent with substantial temperature variance production by the background gradient and local destruction. The decrease in χ below the interface depth is consistent with a weaker temperature gradient compared to the interface.

Profiles of ε and χ are similar in vertical structure, and both show a gradual increase with depth towards the turbulent plume. There are differences in the turbulent interfacial layer and the bottom layer, however. A pronounced peak is observed in χ at the interface in contrast to ε that is relatively constant within $\pm$100 m of the interface depth. Below this level, ε remains high, while χ decreases towards the bottom with respect to the interface depth. In the bottom 100 m, χ remains fairly uniform, whereas ε_N increases. Current shear remains strong below the interface, while the temperature variance is reduced due to the weaker background temperature gradient in the quasi well-mixed bottom layers. In the limiting case of very well-mixed homogeneous bottom layer, the stratified temperature variance model breaks down. Survey-averaged profiles of temperature and velocity inferred from CTD/LADCP stations show that the maximum vertical temperature gradient is located at the interface whereas the velocity shear maximum is approximately 25 m above (not shown). The mean velocity profile has a maximum at approximately 20 m below the interface, corresponding to a minimum in shear, hence local shear production of TKE. This is likely the main reason for the difference

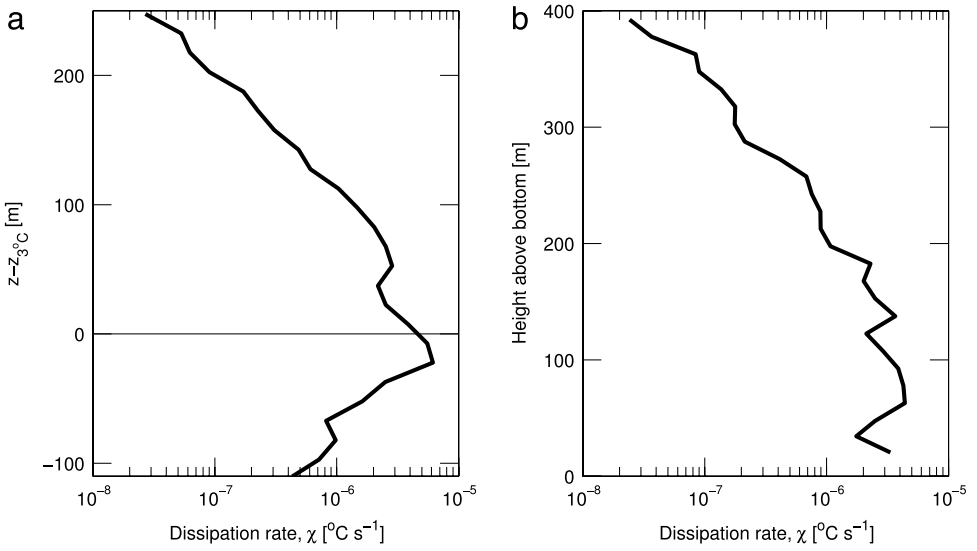

Fig. 9. Survey-averaged profiles of χ. Data are averaged vertically in 15 m bins with respect to (a) the 3 °C isotherm, indicative of the dense plume interface, and (b) height above bottom (HAB).

between the ε and χ profiles at the interface, however, buoyancy effects and anisotropy can also be important.

6.2.2. Probability distributions

Probability distributions of measured ε are shown in Fig. 10, for all data, as well as for three temperature range subsets, corresponding to the dense overflow ($T < 3$ °C), the interfacial layer (3 °C $< T <$ 6 ° C) and the ambient layer (6 °C $< T <$ 9 °C). For the sake of comparison, $\varepsilon_N > 2 \times 10^{-7}$ W kg^{-1} are excluded to be consistent with $\varepsilon_{B,K}$. Compared to ε_N, measured by the shear probes, ε_B and ε_K, measured by the thermistors, show a narrower distribution with relatively more frequently observed intermediate dissipation rates, and less frequent low dissipation rates. The 3–6 °C range is where both ε_B and ε_K deviate the most from ε_N, in the high dissipation tail of the distribution. The distributions of ε_B and ε_K are very similar, except that, although in the same ε band, the peak values for $T < 6$ °C have approximately 5% more contribution in ε_B.

6.2.3. Individual profiles

The survey-averaged profiles of ε_N and ε_B compare very well (Fig. 8). Since they are sampled from the same platform, individual profiles can be contrasted. Two example profiles, one dive and one climb, are shown in Fig. 11. The profiles of ε and χ are averaged in 15 m bins. Profiles of ε_B follow ε_N closely, indicating a very good agreement between the two methods. (Profiles from the Kraichnan model, ε_K, similarly agree with the shear-probe results, ε_N, not shown for clarity.) This is generally the case for all individual profiles. A tendency to underestimation of ε_B is seen when ε_N approaches $\sim 10^{-7}$ W kg^{-1}. Close to the bottom, many data segments are missing (see the bottom 100 m in Figs. 11(e)–(h)), mainly because $\varepsilon > 2 \times 10^{-7}$ W kg^{-1}. In the upper part of the water column the glider flight properties (U, w_g and AOA, Figs. 11(c), (d), (g) and (h)) are relatively smooth. As the glider crosses the plume interface there is substantial variance in glider speed and AOA which persists in the turbulent, highly-sheared bottom boundary layer.

To further investigate similarities and differences between individual ε_N and ε_B, profiles, a scatterplot of ε_N and ε_B is shown in Fig. 12, color coded for temperature. Both variables are averaged vertically in 15 m bins. Data points are excluded when there are less than 5 data points in a given bin, or when the mean temperature gradient in the bin is positive (i.e., unstable over the whole segment).

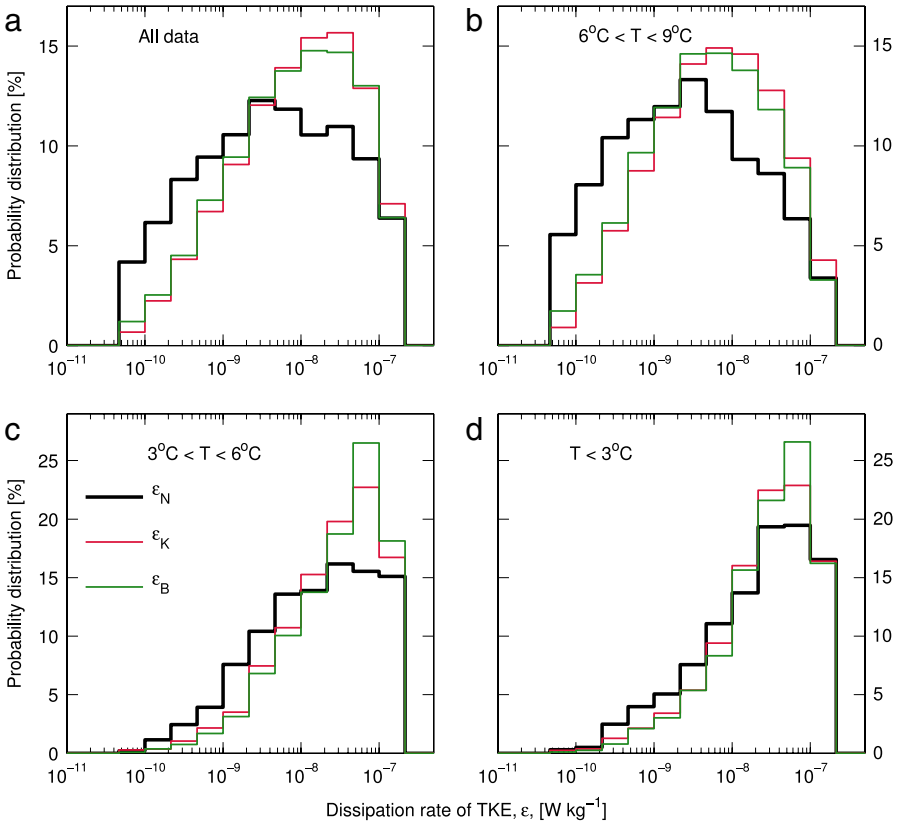

Fig. 10. Probability distribution functions of ε, obtained from the Batchelor (ε_B, green), Kraichnan (ε_K, red) and Nasmyth (ε_N, black) forms. In (a), all data ($\varepsilon < 2 \times 10^{-7}$ W kg^{-1}) are included, while the rest are conditionally sampled for temperature classes (b) 6 °C $< T <$ 9 °C, (c) 3 °C $< T <$ 6 °C and (d) $T <$ 3 °C. (For interpretation of the references to color in this figure legend, the reader is referred to the web version of this article.)

85% of the data points agree to within a factor of $(2^2+2^2)^{1/2} = 2.8$, corresponding to propagation of a factor of two error in both variables. Dissipation rates $\varepsilon > 2\times10^{-7}$ W kg^{-1} and $\varepsilon < 5\times10^{-11}$ W kg^{-1} are removed in the data screening. Still, a tendency towards underestimation of ε_B can be observed for large ε_N, which is also associated with cold water. However, this is often within the typical (factor of two) uncertainty of the data.

6.3. Dissipation flux coefficient

The dissipation flux coefficient, Γ, is commonly used to infer eddy diffusivity, and hence turbulent buoyancy or heat fluxes, from measurements of ε. When both ε and χ are measured simultaneously, an estimate of Γ can be made from

$$\Gamma = \frac{\chi N^2}{2\varepsilon\langle T_z\rangle^2}, \tag{19}$$

(Gargett and Moum, 1995). Ruddick et al. (1997) call this quantity the dissipation coefficient, or apparent mixing efficiency. The flux coefficient is closely related to the mixing efficiency, $R_f = \Gamma/(1+\Gamma)$. From the 15 m vertically averaged dataset, approximately 1100 values of Γ are calculated. Here we use ε_N which is better resolved than $\varepsilon_{B,K}$. (It is here not recommended to infer Γ using thermistor data only.) The distribution of calculated values is shown in Fig. 13. Values span several

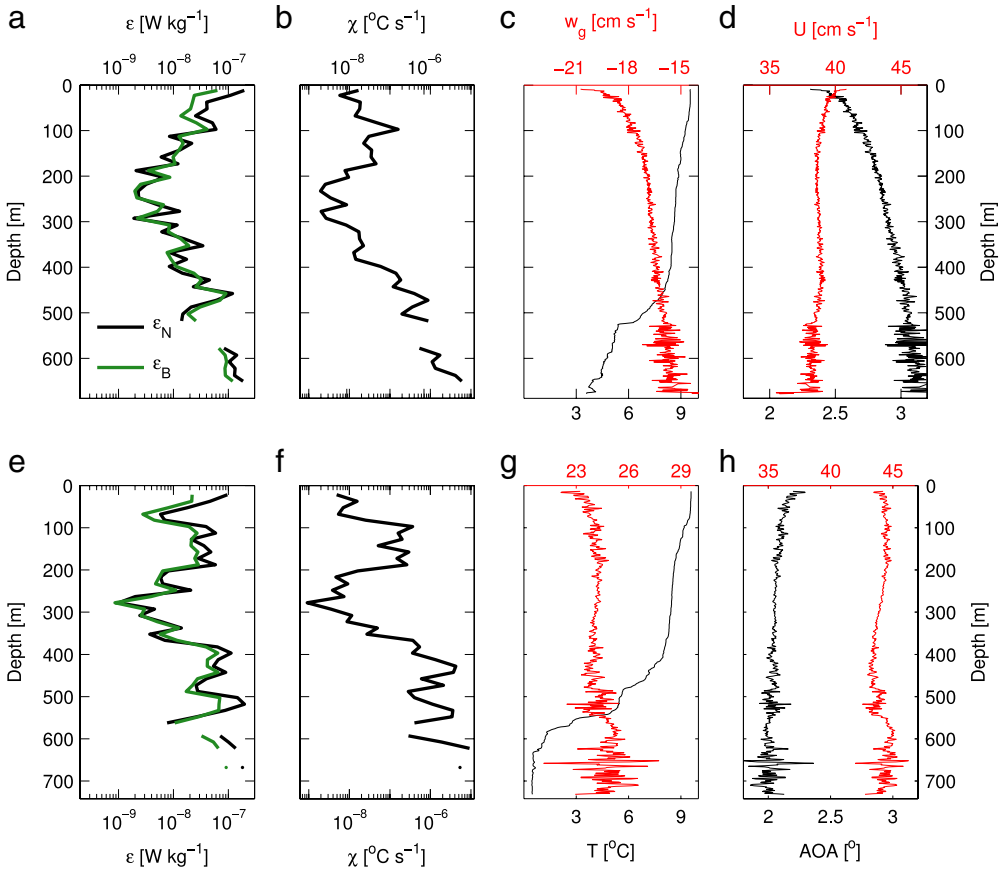

Fig. 11. Two example pseudo-vertical glider profiles, where panels (a) and (e) show the dissipation rate of TKE inferred from shear (ε_N, black) and temperature (Batchelor fit, ε_B, green), panels (b) and (f) show the dissipation rate of thermal variance, χ_B, panels (c) and (g) show vertical glider velocity (w_g, red) and temperature (T, black), and panels (d) and (h) show along-path glider velocity (U, red) and AOA (black). Dissipation rates are averaged in 15-m vertical bins. The upper and lower panels are from one arbitrary deep dive and climb, respectively. (For interpretation of the references to color in this figure legend, the reader is referred to the web version of this article.)

orders of magnitude, but only 9% of the data points lie above 1. The distribution shows a single maximum, and using a bin width of $\frac{1}{30}$, the mode value is 0.14. The geometric mean and the median are both 0.33.

The mixing efficiency has previously been shown to depend on the turbulence activity index, $I_A = \varepsilon/\nu N^2$, which is a commonly used parameter for quantification of turbulence intensity (Shih et al., 2005). We calculated the maximum likelihood estimate of Γ in bins of I_A in the range from 10^0 to 10^5. As seen in Fig. 14, between $I_A = 100$ and $I_A \sim 2 \times 10^4$, there is a steady decrease in Γ for increasing turbulence intensity. Error bars indicate the 95% upper and lower limits of the estimates. The trend in Γ is thus statistically significant. The large error bars at the high and low ends of I_A reflect that fewer values are available for the calculations in those bins. The measurement uncertainty of an individual Γ estimate can be larger than the statistical uncertainties as a result of the typical a factor of two uncertainty in dissipation measurements. The dissipation flux coefficient values, however, are most meaningful in the average sense, averaged over life span of many turbulent eddies. Averaging reduces the errors associated with the dissipation measurements. Although not formally calculated, the accuracy of bin-averaged Γ is estimated to be comparable to the error bars in Fig. 14.

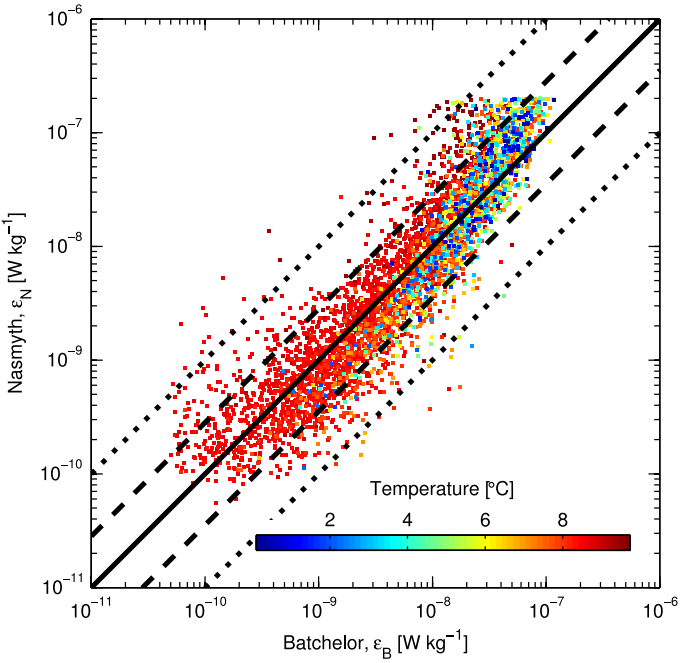

Fig. 12. Comparison of dissipation rates of TKE derived from the Batchelor fits (ε_B) and the shear probes (Nasmyth, ε_N). Markers are color coded for temperature. The solid line represents a one-to-one agreement, the dashed and dotted lines mark deviations of factors 2.8 and 10, respectively.

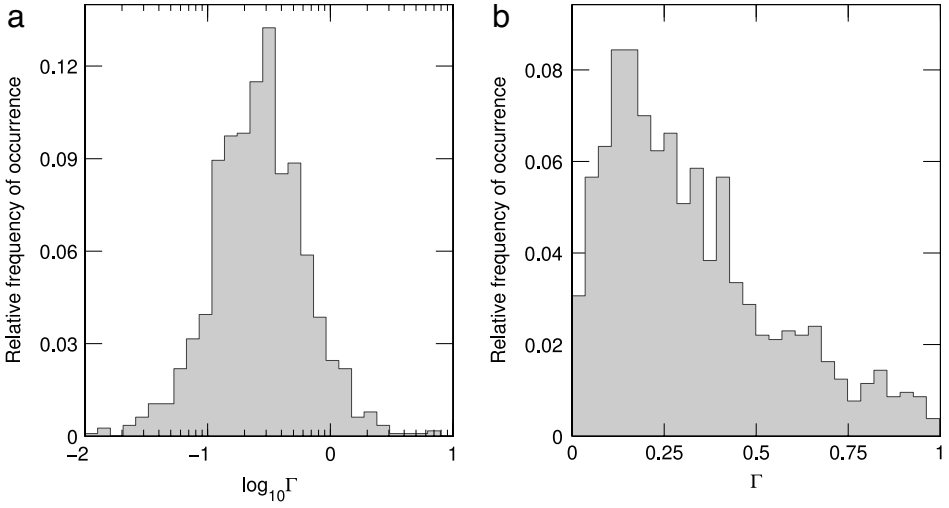

Fig. 13. Probability distribution of the dissipation flux coefficient Γ, shown in (a) 30 logarithmically-spaced bins between 10^{-2} and 10^{1}, and (b) in 30 linearly-spaced bins between 0 and 1. The mode value is 0.14 (using a bin width of $\frac{1}{30}$), the median and the geometric mean are both 0.33.

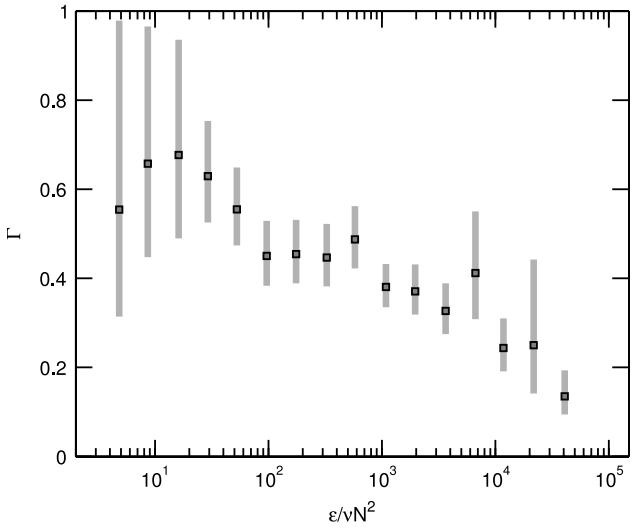

Fig. 14. Dissipation flux coefficient, Γ, versus the turbulence activity index $I_A = \varepsilon/\nu N^2$, calculated as maximum likelihood estimates in bins of I_A. Error bars represent the upper and lower 95% limits of each bin.

7. Discussion

7.1. Glider as a platform for turbulence measurements

Ocean microstructure measurements require sufficient sampling to increase the statistical reliability, and also to average over the inherent intermittency. Furthermore, the methods require a vibration free platform, and specific ranges of speed with which the sensors should move through the water, away from unnatural disturbances and sources of artificial turbulence. The gliders, although not designed for this purpose, are promising platforms that can return high quality and cost-efficient ocean microstructure data.

Caution must be exercised, however, in processing and interpreting the data from gliders. Careful data screening is crucial because there may be portions of the slant profiles which violate the assumptions behind the methods by which the dissipation rates are obtained. Different datasets and environments may call for different criteria and computations for rejection of suspect data. Our dataset is from a challenging oceanographic environment, where the glider experiences navigation difficulties, and it cannot penetrate across the sheared, stratified overflow-ambient interface smoothly and rapidly. Furthermore, the angle of attack and speed of the glider through water must be determined as accurately as possible, necessitating an applicable flight model with site- and glider-specific coefficients. Overall, after data screening, we are left with 75% (shear probes) and 74% (thermistors) of the original dataset. Nevertheless, the amount of data and the quality of the measurements are overwhelming, and can lead to a step increase in our present sampling capabilities and understanding of the ocean mixing processes.

7.2. Dissipation measurements using thermistors

In this study, we utilized two completely independent methods using measurements from shear probes and thermistors to sample the dissipation rate of TKE, ε_N and ε_B (and ε_K), respectively. While the Slocum glider allows easy integration of the MR, gliders fitted with only thermistors are of interest. For this purpose we conducted a detailed comparison of ε measured by the two different methods. The agreement between the two methods lends confidence on the skill of microstructure measurements from gliders, in general, and for the use of thermistors in a limited range of dissipation rates, in particular. A comparison of ε_N and ε_B shows that in segments that are above the noise level, but not very

energetic, the two methods agree to within a measurement uncertainty of a factor of two, for individual segments of 15 m vertical extent. The agreement improves with further averaging. For energetic segments, when dissipation rates exceed $\varepsilon = 2 \times 10^{-7}$ W kg^{-1}, the thermistor's time response correction becomes uncertain, and the temperature gradient spectra are not sufficiently resolved. The turbulent bottom boundary layer (BBL) is one such region where the discrepancy is substantial. Excluding all segments with $\varepsilon > 2 \times 10^{-7}$ W kg^{-1}, from both ε_N and $\varepsilon_{B,K}$, allows a comparison of similarly subsampled datasets. The comparison of the subsampled data shows very good agreement, with discrepancy less than 2% when averaged with respect to the 3 °C isotherm depth, or 15% with respect to HAB. Although this agreement demonstrates the capability of thermistors to measure ε, the discrepancy from the actual (not subsampled) ε profile can be large for energetic turbulence. For $\varepsilon_N \sim 10^{-7}$ W kg^{-1}, ε_B underestimates by a factor of 2, and for $\varepsilon_N \sim 10^{-6}$ W kg^{-1}, the discrepancy reaches one order of magnitude.

The MLE fits of Batchelor and Kraichnan models to observations were generally very good, as demonstrated for individual segments in Fig. 4. In a comparison of the Batchelor and the Kraichnan spectral fits, Sanchez et al. (2011) found that the Kraichnan form gave a better fit to their data, and that the Batchelor fit underestimated at high wavenumbers. In the energetic segment shown in Fig. 4, the Kraichnan form is in slightly better agreement with observations than the Batchelor form. The Kraichnan model does not always give the best fit, however, and in the survey-averaged profiles (Fig. 8), these differences are not apparent. High wavenumbers dominate in the turbulent bottom boundary layer, and based on the findings of Sanchez et al. (2011), ε_B could be expected to underestimate compared to ε_K in the survey-averaged profiles. This is, however, not observed. In our dataset the choice of spectral fit to the temperature variance spectra does not appear to influence the final results significantly. The mean profiles of ε_B and ε_K are identical within the measurement uncertainty.

Oakey (1982) reported ε from both thermistors and shear probes, using the microstructure profiler OCTUPROBE II. He concluded that the two measurement techniques agree to within a factor of 2 on average, similar to our results. It should be noted that his analysis is limited to 25 segments of microstructure measurements. The dataset does not include $\varepsilon > 5 \times 10^{-7}$ W kg^{-1}, consistent with our approach (to exclude unresolved ε). Our results can also be compared to Kocsis et al. (1999), who reported measurements of ε from current shear and temperature microstructure in the surface layer of a lake. Similar to our observations (Fig. 12), Kocsis et al. (1999) found agreement between the two methods to be within a factor of 2 for the bulk of the measurements, but under certain circumstances, discrepancies up to a factor of 10 were observed. They attributed these features to the spatial resolution of the temperature microstructure data, and the noise levels of the shear probes. Note that the measurements by Kocsis et al. (1999) were made using two independent ideal instrumentations and sampling schemes required by the two different methods (shear and temperature microstructure measurements). Their results show that ε is overestimated by the thermistors for low turbulence, and underestimated for energetic turbulence, similar to what is observed in Fig. 10. Considering their dataset and results as state-of-the-art, we conclude that the glider measurements are of comparable quality.

As the turbulent activity index I_A decreases, buoyancy effects become increasingly more important and velocity fluctuations become anisotropic. In such conditions, typical in the $T > 3$ °C range (see Fig. 13(b) of Fer et al. (2014)), we observe a substantial bias in the ratio $\varepsilon_B/\varepsilon_N$. When averaged over ensembles with $I_A < 100$ (where anisotropy is expected), $\varepsilon_B/\varepsilon_N = 2.4$, whereas in the range $100 < I_A < 10^4$, $\varepsilon_B/\varepsilon_N \sim 1$. This leads to a skewness in the probability distribution as seen in Fig. 10. This may be attributed to our use of constant q_B. Several studies left q_B as a free parameter and determined it individually for each patch (see e.g. Nash and Moum, 2002). Gargett (1985) reported a large difference in q_B between isotropic ($q_B = 12$) and anisotropic ($q_B = 4$) temperature gradient spectra. The quality of dissipation measurements from thermistors and the comparison with ε_N can perhaps be improved if q_B is determined for each individual spectrum. This, however, is not tested in the present study.

7.3. Flux coefficient

Smyth et al. (2001) studied the time evolution of the flux coefficient using numerical simulations, which showed that Γ varied by more than one order of magnitude over the lifetime of a turbulent overturn. With time, it approached the asymptotic value of 0.2. Our measurements show a wide range

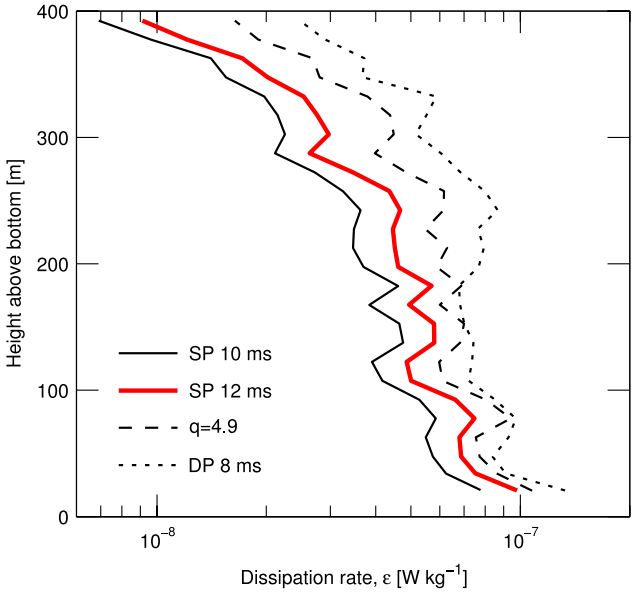

Fig. 15. Sensitivity of survey-averaged ε_B profiles to time response corrections; single pole with $\tau = 10$ ms, single pole with $\tau = 12$ ms and double pole with $\tau = 8$ ms, and to increased $q_B = 4.9$.

of values for Γ, which likely reflects measurements at different stages in turbulent overturns. Using direct numerical simulations, Shih et al. (2005) showed that the mixing efficiency, R_f, and hence Γ, is related to the turbulent activity index, I_A. Glider-derived values of Γ reported here show a comparable decay with increasing turbulence activity which is significant within the measurement uncertainty.

7.4. Sources of errors and sensitivity to chosen parameters

The frequency response of the FP07 thermistor is uncertain and has been the subject of several studies; see the recent overview and discussion in Sommer et al. (2013) and Bogucki et al. (2012). Typically there are two empirical response functions (single or double pole) used in the literature with varying time constants that can be dependent on the speed of the instrument through water. We have utilized a single pole (SP) response function with a speed dependent time constant in the form of Gregg and Meagher (1995) (see Section 5.2). In a recent study, Sommer et al. (2013) obtained $\tau = 10$ ms with no discernible velocity dependence.

To check the sensitivity to the choice of the time constant, τ, and the type of filter, the entire dataset is reprocessed using SP response $H^2(f) = (1 + (f/f_c)^2)^{-1}$ with $\tau = 10$ ms, and a double pole (DP) response $H^2(f) = (1 + (f/f_c)^2)^{-2}$ with $\tau = 8$ ms. The tested uncertainty of 2 ms in τ is twice the typical variability of $\pm 10\%$ (Gregg and Meagher, 1995). Vertically bin-averaged profiles of ε_B are reproduced and presented in Fig. 15. The sensitivity in profiles of ε_K are very similar, and these are not shown. Consistently, we excluded the unresolved dissipation rates ($\varepsilon > 2 \times 10^{-7}$ W kg^{-1}) before averaging; therefore the differences between the curves in the bottom 100 m (where ε is large) can be biased low.

On the average, relative to the SP with $\tau = 12$ ms, the SP with 10 ms underestimates by a factor of 0.81 (± 0.02, one standard deviation over the data points of the average profile). The DP filter with a response time of 8 ms overestimates by a factor of 1.45 (± 0.30). The increase in the dissipation rate estimates in the DP filter relative to the SP filter is because of the larger correction applied in the attenuation (note the -2 power in DP compared to -1 for SP). The correction used in our study is comparable to the response corrections applied in Kocsis et al. (1999), Bogucki et al. (2012) and Sommer et al. (2013) for the typical glider speed of 0.4 m s^{-1}. The half-power frequency (i.e., the frequency at which the attenuation of the response function is 0.5), for the recommended DP with $\tau = 10$ ms

correction (without speed dependence) by Sommer et al. (2013) is 10.2 Hz, comparable to 9.9 Hz in our correction. We estimate the error in $\varepsilon_{B,K}$ associated with the choice of the time constant and the response function to be less than 50%.

The choice of the parameters q_B and q_K in the theoretical spectral shapes is another source of uncertainty. Although these constants are referred to as universal, the range of variability inferred from observations as well as numerical simulations is large; see the discussions in Gargett (1985) and Sanchez et al. (2011). We have used the commonly accepted values. As a check on the sensitivity to q_B, the entire dataset is reprocessed using $q_B = 4.9$ (instead of 3.7), but retaining the SP response with 12 ms constant. The survey-averaged profile is contrasted to the control profile in Fig. 15. This typical upper range of q_B leads to an overestimate of a factor of 1.34 ($\pm$0.15) on the average. This is consistent with Dillon and Caldwell (1980) who estimated that a percentage error in q_B leads to twice the percentage error in ε. We estimate the error in $\varepsilon_{B,K}$ due to the choice of $q_{B,K}$ to be less than 50%, and more typically on the order of 20%.

In addition to the above sensitivity analysis using the measurements, we inferred variability of ε and χ in MLE fit results utilizing modified forms of the Batchelor spectrum. Our reference case is the Batchelor spectrum with $q_B = 3.7$, with the added measured noise spectrum. For a range of assigned values of ε and χ (set equal) to the theoretical spectrum, we perform the MLE fits using identical procedures as in the actual measurements (e.g., the detection of the upper wavenumber limit and correction for the unresolved variance). In the first set of runs, we first attenuate the Batchelor spectrum using the SP, $\tau = 12$ ms response function (giving us an uncorrected "measured" spectrum). We then apply the response correction using $\tau = 10$ ms and $\tau = 14$ ms (each SP), and obtain the MLE fit results. The ratio of resulting dissipation rates to the assigned values ($\varepsilon_{Bobs}/\varepsilon_B$ and χ_{Bobs}/χ_B) are shown in Figs. 16(a) and (b). Over the entire range of ε, a $\pm$2 ms error in τ overestimates and underestimates, respectively, ε by 19% on average. This is similar to the 19% underestimation in ε when $\tau = 10$ ms is used in the observations (Fig. 15). The error in χ is small for weakly energetic turbulence and increases approximately lineary up to about 30% at 10^{-6} W kg^{-1}. Finally we repeated the analysis, but this time changing q_B; we tested $q_B = 3$ and 5 (20% smaller and 35% larger than $q_B = 3.7$). The results are shown in Figs. 16(c) and (d) for ε and χ, respectively. The resulting error in χ is negligible (<2%); the error in ε, on the other hand, is on average 49% and 45% for $q_B = 3$ and $q_B = 5$, respectively. These figures are again consistent with those inferred from the actual measurements (Fig. 15). The drop in the $\varepsilon_{Bobs}/\varepsilon_B$ ratio at large values of ε for $q_B = 3$ is due to our imposed 200 cpm upper wavenumber cut-off for the range to fit the spectrum.

The errors associated with the optimized coefficients, C_{D_0}, c_h, and V_g will propagate into AOA, the glider speed through water, and the resulting dissipation measurements (both from shear probes and from thermistors). We have reprocessed the dataset by assigning $\pm$20% variability (chosen arbitrarily) in C_{D_0} and the hull compressibility, i.e. using $0.8C_{D_0}$, $1.2C_{D_0}$ and $1.2c_h$. The glider volume is typically obtained to within a few percent, and is not tested. After data screening (Section 5.3), the ratio of the AOA, U and ε values for the test case to the standard case are calculated. The average and standard deviation of this ratio is interpreted as the error in ε. A 20% error in C_D leads to approximately 19($\pm$1)%, average error in AOA, for both dives and climbs. The corresponding error in U is 9($\pm$2)%. Compressibility does not affect the AOA, but leads to 6($\pm$3)% error in U, similar in dives and climbs. The error apparent in ε is similar for dives and climbs: for $1.2C_{D_0}$, about 40($\pm$30)%, i.e. with large variability, and for $0.8C_{D_0}$, 40($\pm$10)%, i.e. with less variability. Dissipation rates measured in dives are less affected by the error in compressibility, with 18($\pm$10)%, compared to 30($\pm$25)% in climbs. When vertically averaged ($dz = 15$ m) values are contrasted, the error in ε and its variability associated with C_{D_0} decreases substantially for dives (to 18%) and remains about 40($\pm$4)% for climbs. Overall we attribute less than 50% error in dissipation measurements as a result of uncertainties in the hydrodynamic flight model parameters.

In summary, the above analysis suggests that errors (in ε) associated with the choice of q, the response correction and the flight model calculations are each less than 50%.

8. Conclusions

Dissipation rates of turbulent kinetic energy (ε) and temperature variance (χ) have been measured using an autonomous underwater glider equipped with microstructure sensors, deployed in the

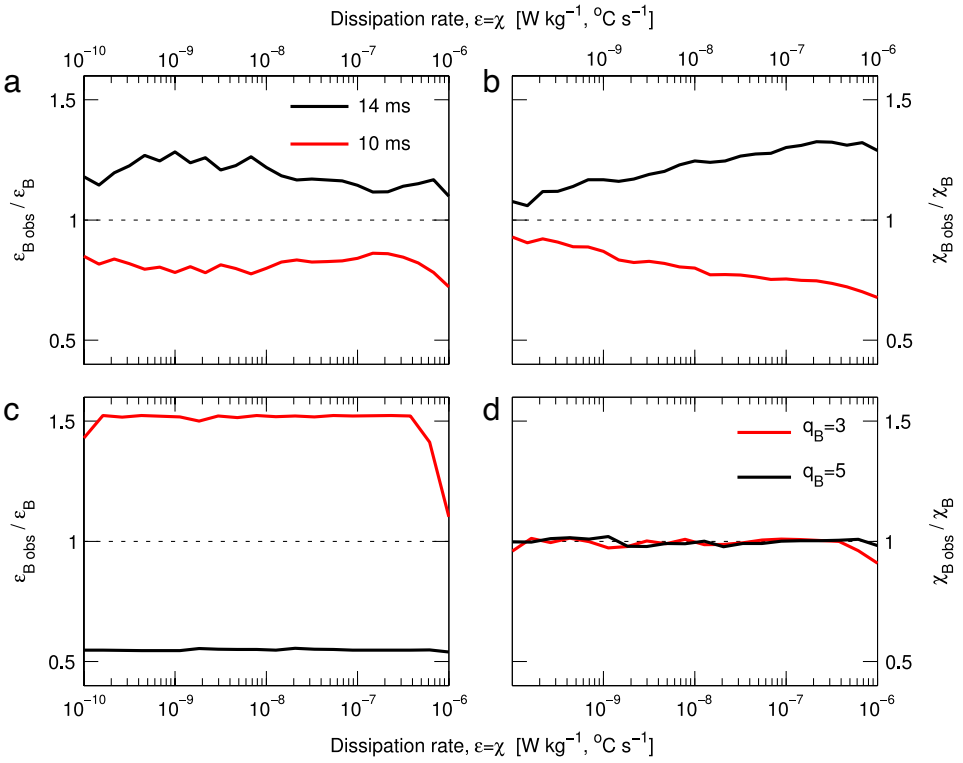

Fig. 16. Sensitivity of ((a) & (c)) ε_B and ((b) & (d)) χ_B to ((a) & (b)) thermistor response time $\tau = 12 \pm 2$ ms and ((c) & (d)) the fitting coefficient $q_B = 3$ and $q_B = 5$ relative to $q_B = 3.7$.

Faroe Bank Channel. This site is home to a turbulent deep overflow beneath a relatively quiescent ambient. Both the shear probes and the thermistors have been used to measure ε, which provided two independent measurements from the same platform. Shear variance in the part of the observed shear spectra which is not contaminated by noise is integrated, and the unresolved part is accounted for by using the Nasmyth's empirical form. Temperature gradient variance spectra are fitted, using a maximum likelihood method, to the theoretical spectra of Batchelor and Kraichnan. Careful data screening is required to identify and remove portions of the glider's slant profiles which violate the assumptions behind the methods. Different datasets and environments may call for different criteria and computations for rejection of suspect data.

The resulting temperature-derived ($\varepsilon_{B,K}$) and shear-derived (ε_N) dissipation rates agree very well up to $\varepsilon \sim 10^{-7}$ W kg^{-1}, both in individual and survey-averaged profiles. Comparison of survey-averaged profiles subsampled for $\varepsilon < 2 \times 10^{-7}$ W kg^{-1} shows agreement to within 2% and 15% when averaged with respect to the plume interface depth and height above bottom, respectively. Contrary to the thermistor-derived $\varepsilon_{B,K}$, the shear-derived ε_N resolves the high dissipation rates, and comparison with the actual (not subsampled) ε_N reveals substantial discrepancies in turbulent waters; $\varepsilon_{B,K}$ is underestimated by a factor of 2 at $\varepsilon_N \sim 10^{-7}$ W kg^{-1}, and by a factor of 10 at $\varepsilon_N \sim 10^{-6}$ W kg^{-1}. Probability distribution functions show that $\varepsilon_{B,K}$ underestimates low dissipation rates and overestimates intermediate dissipation rates compared to ε_N. In low or intermediately energetic environments, measuring dissipation rates using thermistors on gliders is possible. Using only thermistors for measurements of dissipation rates is not recommended for very turbulent sites, including e.g. the upper mixed layer; although χ is relatively better resolved, ε is underestimated.

The dataset is further utilized to calculate the dissipation flux coefficient, Γ. Despite the large variability, the mode value is $\Gamma = 0.14$, and the median and geometric mean are 0.33, not far from the

commonly used value of $\Gamma = 0.2$. When averaged in bins of a turbulent activity index parameter, Γ decays with increasing turbulence activity. The decrease in Γ is significant at the 95% confidence level.

Sensitivity tests have been performed to evaluate the error propagation to dissipation measurements following an error in the choice of parameters and calibration coefficients in our methods. Errors in ε associated with the choice of the fitting parameter q, thermistor response correction and the glider flight model calculations are each less than 50%. Overall, we conclude that dissipation measurements using thermistors on a glider are good to within a factor of two up to an upper limit of $\varepsilon \sim 10^{-7}$ W kg^{-1}. A factor of two uncertainty is typical of ocean microstructure measurements using microstructure profilers.

Gliders prove to be a very useful contribution for sampling ocean microstructure. The two independent measurements of dissipation rates compare well for typical oceanic turbulence levels, indicating that measurements from gliders are reliable enough to be used for studies of ocean mixing processes. Using gliders as a supplement to shipborne microstructure profilers can greatly improve sampling of mixing in the ocean at lower cost.

Acknowledgments

This work has been funded by the Research Council of Norway, through the FRINAT program, under the project "Faroe Bank Channel Overflow: Dynamics and Mixing". The authors thank Jenny E. Ullgren, Lucas Merckelbach, Gerd Krahmann, the crew on R/V Håkon Mosby and participants in the field work. Comments from two reviewers greatly improved an earlier version of the manuscript.

References

Batchelor, G.K., 1959. Small-scale variation of convected quantities like temperature in turbulent fluid. Part 1: general discussion and the case of small conductivity. J. Fluid Mech. 5 (1), 113–133.

Beaird, N., Fer, I., Rhines, P., Eriksen, C., 2012. Dissipation of turbulent kinetic energy inferred from seagliders: an application to the eastern Nordic Seas overflows. J. Phys. Oceanogr. 42, 2268–2282.

Bogucki, D., Luo, H., Domaradzki, J., 2012. Experimental evidence of the Kraichnan scalar spectrum at high Reynolds number. J. Phys. Oceanogr. 42, 1717–1728.

Darelius, E., Fer, I., Quadfasel, D., 2011. Faroe Bank Channel overflow: mesoscale variability. J. Phys. Oceanogr. 41 (11), 2137–2154.

Darelius, E., Ullgren, J.E., Fer, I., 2013. Observations of barotropic oscillations and their influence on mixing in the Faroe Bank Channel overflow region. J. Phys. Oceanogr. 43 (7), 1525–1532.

Dillon, T.M., Caldwell, D.R., 1980. The Batchelor spectrum and dissipation in the upper ocean. J. Geophys. Res. 85 (NC4), 1910–1916.

Fer, I., Peterson, A.K., Ullgren, J.E., 2014. Microstructure measurements from an underwater glider in the turbulent Faroe Bank Channel overflow. J. Atmos. Ocean. Technol. 31 (5), 1128–1150.

Fer, I., Voet, G., Seim, K.S., Rudels, B., Latarius, K., 2010. Intense mixing of the Faroe Bank Channel overflow. Geophys. Res. Lett. 37, L02604.

Gargett, A.E., 1985. Evolution of scalar spectra with the decay of turbulence in a stratified fluid. J. Fluid Mech. 159, 379–407.

Gargett, A.E., Moum, J.N., 1995. Mixing efficiencies in turbulent tidal fronts—results from direct and indirect measurements of density flux. J. Phys. Oceanogr. 25 (11), 2583–2608.

Gregg, M.C., Meagher, T.B., 1980. The dynamic response of glass rod thermistors. J. Geophys. Res. 85, 2779–2786.

Gregg, M.C., Seim, H.E., Percival, D.B., 1993. Statistics of shear and turbulent dissipation profiles in random internal wave-fields. J. Phys. Oceanogr. 23 (8), 1777–1799.

Hansen, B., Østerhus, S., 2007. Faroe Bank Channel overflow 1995–2005. Prog. Oceanogr. 75 (4), 817–856.

Johnson, G.C., Sanford, T.B., 1992. Secondary circulation in the Faroe Bank Channel outflow. J. Phys. Oceanogr. 22 (8), 927–933.

Jones, C., Creed, E., Glenn, S., Kerfoot, J., Kohut, J., Mudgal, C., Schofield, O., 2005. Slocum gliders—A component of operational oceanography. In: Proceedings of 14th International Symposium on Unmanned Untethered Submersible Technology (UUST).

Kocsis, O., Prandke, H., Stips, A., Simon, A., Wüest, A., 1999. Comparison of dissipation of turbulent kinetic energy determined from shear and temperature microstructure. J. Mar. Syst. 21 (1–4), 67–84.

Kraichnan, R., 1968. Small-scale structure of a scalar field convected by turbulence. Phys. Fluids 11 (5), 945–953.

Lueck, R.G., Wolk, F., Yamazaki, H., 2002. Oceanic velocity microstructure measurements in the 20th century. J. Oceanogr. 58 (1), 153–174.

Luketina, D.A., Imberger, R., 2001. Determining turbulent kinetic energy dissipation from Batchelor curve fitting. J. Atmos. Ocean. Technol. 18 (1), 100–113.

McDougall, T., Barker, P., 2011. Getting started with TEOS-10 and the Gibbs Seawater (GSW) Oceanographic Toolbox. SCOR/IAPSO WG127.

Merckelbach, L., Smeed, D., Griffiths, G., 2010. Vertical water velocities from underwater gliders. J. Atmos. Ocean. Technol. 27, 547–563.

Nash, J., Caldwell, D., Zelman, M., Moum, J., 1999. A thermocouple probe for high-speed temperature measurement in the ocean. J. Atmos. Ocean. Technol. 16, 1474–1482.
Nash, J.D., Moum, J.N., 2002. Microstructure estimates of turbulent salinity flux and the dissipation spectrum of salinity. J. Phys. Oceanogr. 32, 2312–2333.
Nasmyth, P., 1970. Oceanic Turbulence (Ph.D. thesis). University of British, Columbia.
Oakey, N., 1982. Determination of the rate of dissipation of turbulent energy from simultaneous temperature and velocity shear microstructure measurements. J. Phys. Oceanogr. 12, 256–271.
Peters, H., Gregg, M., Toole, J., 1988. On the parameterization of equatorial turbulence. J. Geophys. Res.: Oceans 93 (C2), 1199–1218.
Ruddick, B., Anis, A., Thompson, K., 2000. Maximum likelihood spectral fitting: the Batchelor spectrum. J. Atmos. Ocean. Technol. 17 (11), 1541–1555.
Ruddick, B., Walsh, D., Oakey, N., 1997. Variations in apparent mixing efficiency in the North Atlantic central water. J. Phys. Oceanogr. 27 (12), 2589–2605.
Sanchez, X., Roget, E., Planella, J., Forcat, F., 2011. Small-scale spectrum of a scalar field in water: the Batchelor and Kraichman models. J. Phys. Oceanogr. 41, 2155–2167.
Seim, K.S., Fer, I., 2011. Mixing in the stratified interface of the Faroe Bank Channel overflow: the role of transverse circulation and internal waves. J. Geophys. Res. 116 (C07), C07022.
Shih, L.H., Koseff, J.R., Ivey, G.N., Ferziger, J.H., 2005. Parameterization of turbulent fluxes and scales using homogeneous sheared stably stratified turbulence simulations. J. Fluid Mech. 525, 193–214.
Smyth, W.D., Moum, J.N., Caldwell, D.R., 2001. The efficiency of mixing in turbulent patches: inferences from direct simulations and microstructure observations. J. Phys. Oceanogr. 31 (8), 1969–1992.
Sommer, T., Carpenter, J.R., Schmid, M., Lueck, R.G., Wüest, A., 2013. Revisiting microstructure sensor responses with implications for double-diffusive fluxes. J. Atmos. Ocean. Technol. 30 (8), 1907–1923.
Thorpe, S.A., 2007. An Introduction to Ocean Turbulence. Cambridge University Press.
Ullgren, J.E., Fer, I., Darelius, E., Beaird, N., 2014. Interaction of the Faroe Bank Channel overflow with Iceland Basin intermediate waters. J. Geophys. Res.: Oceans 119 (1), 228–240.
Wolk, F., Lueck, R., St. Laurent, L., 2009. Turbulence measurements from a glider. In: Marine Technology for Our Future: Global and Local Challenges. MTS/IEEE, MTS/IEEE pp. 1–6.